



ELSEVIER

Contents lists available at ScienceDirect

Electrochimica Acta

journal homepage: www.elsevier.com/locate/electacta

Modeling electrode-level crack and quantifying its effect on battery performance and impedance

Tianhan Gao^a, Andrew Kim^a, Wei Lu^{a,b,*}^a Department of Mechanical Engineering, University of Michigan, Ann Arbor, MI 48109, USA^b Department of Materials Science and Engineering, University of Michigan, Ann Arbor, MI 48109, USA

ARTICLE INFO

Article history:

Received 13 July 2020

Revised 11 September 2020

Accepted 27 September 2020

Available online 6 October 2020

Keywords:

Lithium ion battery

Crack

Ion transport

Intercalation

Cell performance

Impedance

ABSTRACT

Electrode-level cracks in a Li ion battery significantly impact its performance. We build a crack-containing electrochemical model to reveal the mechanism and quantify the effect of crack geometrical characteristics on specific energy, specific capacity and cell impedance. An elliptical-shaped crack is introduced into the electrode, which represents various configurations by changing the semi-axis ratio, crack angle and crack position. We show that lithium ion transport, electrochemical intercalation and the overall cell impedance are sensitive to the crack characteristics and electrotype absorption on crack surfaces. A longer crack more parallel to the current collector reduces the specific energy and specific capacity more significantly, especially when the current density is high. By contrast, a crack perpendicular to the current collector has little impact. The dependence on a series of crack orientation is quantified. The study of crack position shows that a crack closer to the separator has a stronger negative impact, dramatically reducing capacity. Electrochemical impedance spectroscopy simulations show that the crack shape factors such as semi-axis ratio, crack angle and electrolyte wetting ratio primarily affect the ohmic resistance. A longer crack more parallel to the current collector increases the ohmic resistance, while more crack wetting reduces the ohmic resistance. By contrast, crack position significantly affects the charge transfer resistance but with little impact on the ohmic resistance. A crack closer to the separator increases the charge transfer resistance. The effect of connected cracks into an open or closed ring shape is also considered, which can partially isolate active materials from the electrode depending on the size and orientation of the opening. This work provides a comprehensive and fundamental understanding of how various crack geometrical parameters affect the electrochemical behavior, which can assist in evaluating the significance of cracking, allow comparison with other degradation mechanisms to identify the limiting factor, and provide guidance on battery design and application strategy.

© 2020 Elsevier Ltd. All rights reserved.

1. Introduction

Lithium-ion batteries (LIBs) are widely used in many fields such as electrical vehicles, commercial electronic products and space applications because of their high energy storage capability. However, they can suffer severe capacity degradation over time as a result of repeated charge/discharge cycles during usage. Multiple mechanisms such as electrolyte degradation [1,2], electrode material dissolution and solid electrolyte interphase (SEI) formation [3,4], lithium plating and dendrite formation [5–7] may contribute to battery cell degradation. Characteristics such as specific energy, specific power, specific capacity [8] and electrochemical impedance [9] are commonly used to quantify the effect of degradation. Crack-

ing in the electrode is known to be a major degradation mechanism. This mechanism becomes critical especially for high capacity electrodes which experience more volume change during lithium intercalation/intercalation, and for high rate applications or fast charging conditions where the high current density induces a larger stress in the electrodes.

Cracking can occur in the form of microcracks inside an active material particle, or in the form of electrode-level cracks by debonding between particles [10–12], inappropriate drying during the manufacturing process [13], or electrode delamination from the current collector [14]. Currently, most studies focused on investigating the crack growth process. For instance, at the particle-level, Zhang et al. [15] investigated the intra-particle fracture within the secondary particle based on cohesive crack modeling. Klinsmann et al. [16] investigated the effect of particle size and applied boundary flux on crack formation using a phase-field model. Tahmasbi and Eikerling [17] developed a statistical physical-based

* Corresponding author.

E-mail address: weilu@umich.edu (W. Lu).

model to study the mechanical degradation in Li-ion batteries. For electrode-level cracks, Vanpeene et al. [18] used in-situ X-ray tomography to investigate the 3-D morphological evolution of a silicon-based electrode and crack propagation with the cycle number. Lee et al. [19] developed an integrated electrochemical-mechanical and cohesive zone model to simulate the debonding of active material particles from the binder during lithium intercalation. Bhandakkar and Gao [20] studied crack nucleation in an initially crack-free electrode during galvanostatic intercalation and deintercalation with a cohesive model. These studies have advanced the understanding of crack initiation and growth in an electrode. However, how to systematically quantify the effect of crack on the overall cell performance still remains to be studied.

Modeling and quantifying various crack configurations on cell performance will provide critical information on the significance of crack under various situations, allow comparison with other degradation mechanisms to identify the limiting process, and provide important guidance on battery design and application strategy. So far, most work studying the consequence of crack relied on experimental approaches. When studying the role of binding materials on the mechanical behavior and crack resistance of silicon electrodes during cycling, Lee et al. [10] captured the electrode-level crack morphology after various number of cycles and compared the capacity. They showed that the cycle life can be improved by a binder with moderate elasticity. Nagulapati et al. [11,12] investigated the type of binding material on the performance of a sodium-ion battery. They compared the characteristics of electrode crack formation with different type of binders and investigated the change of capacity and impedance with the cycle number. Studying the capacity fade of a porous NiO/Ni foam electrode, Rahman and Wen [21] visualized cracks in the electrode and correlated the change of capacity and cell impedance to the cycle number. Wang et al. [22] investigated crack formation and evolution in silicon-composite electrodes with different binders, and showed decreasing capacity with cycle numbers. Zhao et al. [23] characterized the Li ion transport rate parallel and perpendicular to the silicon-carbon interface in an amorphous Si/C multilayer electrode. They captured the morphology of electrode-level crack after different number of cycles with SEM, and correlated the electrode-level crack area to the apparent diffusion coefficient of Li ions.

These studies have shown that crack morphology directly and strongly affects typical cell performance indicators such as specific capacity and specific energy as well as cell impedance. However, it is difficult to experimentally quantify the relationship between the electrode-level crack geometry and cell performance and impedance because of the challenge to distinguish the effect of multiple cracks, to capture the local electrochemical process, and to isolate the effect of capacity degradation from concurrent mechanisms, such as mechanical stress [24], SEI growth [25], electrolyte decomposition [1] and other side reactions [3,4], since all these factors can contribute to the change of cell performance and impedance. In addition, it is difficult to accurately control the crack geometries for comparison. Thus, we use a computational approach to systematically study and quantify the effect of crack geometry on cell performance. In addition, our model and simulation will provide new insights on the underlying electrochemical processes such as ion transport and local state of charge under the influence of cracks, which cannot be easily obtained experimentally.

Finite element (FE) simulation coupled with electrochemical modeling [26] is a powerful approach for battery studies. Finite element analysis (FEA) can capture the electrochemical characteristics within the cell, such as local state of charge, ion transport, and concentration and potential distribution within an electrode [27]. Yang et al. [28] numerically studied the electrochemical and stress field coupling effect inside a pre-cracked silicon-film. They

especially focused on the lithium gathering mechanism and stress relaxation phenomenon around the crack tip. Xu and Zhao [29] calculated the corrosive fracture of electrodes under concurrent mechanical and chemical load based on a theory of coupled diffusion, large deformation and crack growth. They found that the lithium accumulated at the crack tip appends a local dilatational strain and can reduce the fracture toughness. Gao and Zhou [30] numerically investigated the effect of lithiation-induced fracture by J-integral for a pre-cracked Li/Si thin-film electrode. They found that when the electrode operates at higher Li concentrations, the force for fracture is significantly lower. These work highlight the use of FEA for studying the formation and evolution of electrode-level cracks.

Different from previous studies, here we focus on the impact of crack rather than how crack is formed. The study will provide scientific insights into the relationship between the crack geometrical parameters and the cell performance and impedance, help with the electrode design strategy, and provide information for degradation analysis. For instance, in post-mortem analysis of electrode, one can observe the crack geometry or count the crack length to estimate whether crack is a major contributor to the degradation or failure. With FEA, various crack geometry and location can be studied, allowing connecting the underlying electrochemical process to cell performance and impedance. We introduce an elliptical-shaped electrode-level crack into a pseudo three-dimensional battery model and implement it using COMSOL Multiphysics. The shape can represent various configurations by changing the semi-axis ratio, crack angle, and crack position. We further consider connected cracks into a semi-closed ring shape with various opening sizes and opening directions. We specifically focus on quantifying the impact of crack on the electrochemical properties, including ion transport, intercalation characteristics, capacity and impedance.

2. Model

2.1. Geometry

Fig. 1a shows the setup of a half-cell composed of a lithium metal anode, a separator and a crack-containing cathode. The width (W) of the cell is set to $80\ \mu\text{m}$. The cathode thickness (L) is set to $80\ \mu\text{m}$ and the separator thickness (L_s) is set to $30\ \mu\text{m}$. The crack in the electrode is described by an ellipse. There is no active material inside the crack, but various amount of electrolyte is absorbed on its surface, as shown in Fig. 1b. The electrolyte wetting area is defined by the crack internal area minus the inactive area (assumed to have the same semi-axis ratio as the crack). The amount of electrolyte absorbed is quantified by the wetting ratio (W_R), which is defined as the ratio of the electrolyte wetting area to the whole area inside the crack. $W_R=0$ means that the region inside the crack has no electrolyte, while $W_R=1$ means that the region inside the crack is full of electrolyte. The crack geometrical characteristics are quantified by

- (1) The length ratio of the long semi-axis over the short semi-axis (a/b);
- (2) The angle (θ);
- (3) The central position of the crack (d).

Representative geometries are shown in Fig. 1c.

2.2. Electrochemical modeling

2.2.1. Governing equations

The pseudo three dimensional (P3D) electrochemical model is built on the classic porous electrode theory [26]. The dimensions include x , y (Fig. 1a) and r along the particle radius direction. The

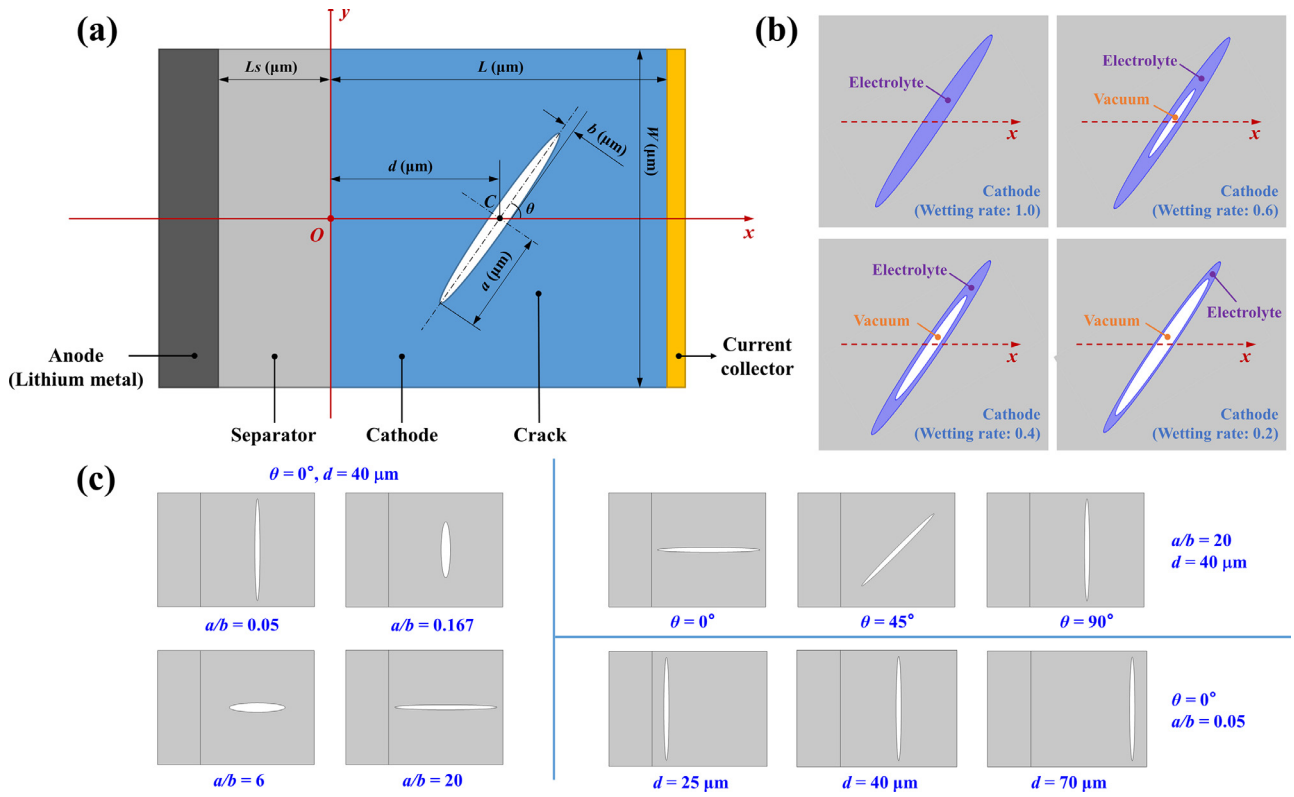


Fig. 1. (a) The setup of a half-cell with a crack in the electrode. (b) A crack with different amount of electrolyte wetting inside the crack. The white region is an open space with no material or electrolyte. (c) Representative crack geometries with different aspect ratio a/b , angle θ and position d .

solid phase potential, Φ_s (V), and electrolyte potential, Φ_e (V) are governed by

$$\nabla \cdot (\sigma_s^{eff} \nabla \Phi_s) = a_s i \quad (1)$$

$$\nabla \cdot \left\{ -\kappa_e^{eff} \left[\nabla \Phi_e - \frac{2RT}{F} \left(1 + \frac{d \ln f_{\pm}}{d \ln c_e} \right) (1 - t_+) \nabla \ln c_e \right] \right\} = a_s i \quad (2)$$

where $\sigma_s^{eff} = \sigma_{s0} \varepsilon_s^{1.5}$ is the effective solid conductivity with σ_{s0} ($S m^{-1}$) being the bulk solid conductivity and ε_s the volume fraction of solid. $a_s = 3\varepsilon_s/r_p$ is the active surface area per unit electrode volume with r_p (m) being the active particle radius. The reaction current density, i ($A m^{-2}$), is given by the Butler-Volmer equation in the electrode region (shown later), and is 0 in the electrolyte region. $\kappa_e^{eff} = \kappa_{e0} \varepsilon_e^{1.5}$ is the effective electrolyte conductivity with κ_{e0} ($S m^{-1}$) being the bulk electrolyte conductivity and ε_e the volume fraction of electrolyte. R ($J mol^{-1} K^{-1}$) is ideal gas constant, T (K) is temperature, and F ($C mol^{-1}$) is Faraday's constant. f_{\pm} is the electrolyte activity coefficient. c_e ($mol m^{-3}$) is the lithium ion concentration in the electrolyte. t_+ is the lithium ion transference number.

The lithium-ion concentration in the electrolyte is given by

$$\varepsilon_e \frac{\partial c_e}{\partial t} + \nabla \cdot (-D_e^{eff} \nabla c_e) = \frac{(1 - t_+)}{F} a_s i, \quad (3)$$

where t (s) is time, $D_e^{eff} = D_{e0} \varepsilon_e^{1.5}$ is the effective diffusivity of the electrolyte with D_{e0} ($m^2 s^{-1}$) being the bulk electrolyte diffusivity.

The electrolyte layer absorbed on the crack surface is accounted for as an additional region of electrolyte (wetting ratio W_R multiplying the crack internal area, as shown in Fig. 1b). The governing equations for lithium ion concentration and electrolyte potential in

the electrolyte wetting area are the same as Eqs. (2) and (3) and with $\varepsilon_e = 1$ and $i = 0$.

The reaction current density between the particle and the electrolyte is governed by the Butler-Volmer equation,

$$i = i_0 \left(\exp \left(\frac{\alpha F \eta}{RT} \right) - \exp \left(-\frac{(1 - \alpha) F \eta}{RT} \right) \right), \quad (4)$$

where the exchange current density, i_0 ($A m^{-2}$), is given by $i_0 = F k c_{s,surf}^{1-\alpha} c_e^\alpha (c_{s,max} - c_{s,surf})^\alpha$. Here α is the anodic charge transfer coefficient, k ($m^{2.5} mol^{-0.5} s^{-1}$) is the reaction rate constant, $c_{s,surf}$ ($mol m^{-3}$) is the lithium ion concentration on the particle surface, and $c_{s,max}$ ($mol m^{-3}$) is the maximum lithium ion concentration inside the particle. The over-potential, η (V), is given by $\eta = \Phi_s - \Phi_e - E_{eq}$ (SOC), where E_{eq} (V) is the equilibrium potential of the cathode material and is a function of state of charge (SOC).

The lithium ion concentration in the active particle is given by

$$\frac{\partial c_s}{\partial t} = \frac{D_s}{r^2} \frac{\partial}{\partial r} \left(r^2 \frac{\partial c_s}{\partial r} \right) \quad (5)$$

where c_s ($mol m^{-3}$) is the lithium ion concentration in the particle and D_s ($m^2 s^{-1}$) is the diffusivity of lithium ion in the particle.

The values of electrochemical parameters used in our simulations are presented in Table A1 and Fig. A1 in Appendix A. f_{\pm} is taken to be a constant so that $d \ln f_{\pm} / d \ln c_e = 0$. For demonstration, we consider $LiMn_2O_4$ (LMO) as the cathode material. The electrolyte is $1000 mol m^{-3} LiPF_6$ in EC:DMC (2:1 wt%). The minimum and maximum cathode SOC are taken to be 0.19 and 0.99, respectively. For the initial condition, the cathode SOC is 0.19 and lithium ion concentration in the electrolyte is $1000 mol m^{-3}$.

2.2.2. Boundary conditions

The boundary conditions next to the current collector ($x=L$) are given by

$$\sigma_s^{eff} \frac{\partial \Phi_s}{\partial x} = -i_{app}, \quad \frac{\partial \Phi_e}{\partial x} = 0, \quad \frac{\partial c_e}{\partial x} = 0, \quad (6)$$

where i_{app} ($A m^{-2}$) is the applied discharge current density on the current collector, setting to be a constant during the discharging process.

The reaction at the lithium metal surface ($x = -L_s$) is given by the Butler-Volmer equation [5],

$$i_{Li} = FK_{Li}(c_e)^{1-\beta} \left(\exp\left(\frac{(1-\beta)F\eta_{Li}}{RT}\right) - \exp\left(-\frac{\beta F\eta_{Li}}{RT}\right) \right), \quad (7)$$

where i_{Li} ($A m^{-2}$) is the current density on the lithium metal surface, K_{Li} ($m^{-0.5} mol^{0.5} s^{-1}$) is the lithium deposition rate coefficient, β is the charge transfer coefficient for lithium deposition, and η_{Li} (V) is the over-potential given by

$$\eta_{Li} = \Phi_{Li} - \Phi_e, \quad (8)$$

where Φ_{Li} (V) is the lithium metal potential and is taken to be $\Phi_{Li}=0$. Since $i_{Li} = i_{app}$, Eqs. (7) and (8) give the expression of Φ_e at $x = -L_s$.

The boundary conditions at $y = \pm 0.5W$ are given by

$$\frac{\partial \Phi_s}{\partial y} = 0, \quad \frac{\partial \Phi_e}{\partial y} = 0, \quad \frac{\partial c_e}{\partial y} = 0. \quad (9)$$

The boundary conditions at the surface of the inactive region (normal direction \mathbf{n}) inside the crack (i.e. at the surface of the wetted electrolyte) are given by

$$\frac{\partial \Phi_e}{\partial n} = 0, \quad \frac{\partial c_e}{\partial n} = 0. \quad (10)$$

The particle-level boundary conditions are

$$\text{at } r = 0: \quad \frac{\partial c_s}{\partial r} = 0, \quad \text{at } r = r_p: \quad D_s \frac{\partial c_s}{\partial r} = -\frac{i}{F}. \quad (11)$$

For the electrochemical impedance spectroscopy (EIS) simulation, a cell is first discharged to a pre-defined average SOC of the cathode, followed by a rest for 5000 s to reach a uniform lithium ion distribution. Then the frequency-domain module in COMSOL is employed to execute the EIS simulation. The capacitance between the particle and the electrolyte is set to be $0.1 F m^{-2}$. For EIS simulation, the solid potential at $x=L$ is given by

$$\Phi_s = E_{eq}(SOC) + \Delta\Phi \sin(2\pi f_{app}t), \quad (12)$$

where $\Delta\Phi$ (V) is the amplitude of applied terminal voltage disturbance taken to be $0.005 V$ and f_{app} (Hz) is the frequency of applied disturbance selected to sweep from $0.1 Hz$ to $10^7 Hz$.

2.2.3. Battery performance characterization

The specific energy (SE) and specific capacity (SC) under various discharge currents are employed to evaluate the cell performance. They are calculated by

$$SE = \frac{\int_0^{t_d} V_t I dt}{m} \quad (13)$$

$$SC = \frac{I t_d}{m} \quad (14)$$

where V_t (V) is the terminal voltage, I (A) is the discharge current calculated by $I=i_{app}A$ with A being the cross-sectional area of the electrode, and t_d denotes the time (s) when discharging ends. The discharging process ends when V_t reaches the cutoff voltage. We consider several cutoff voltage scenarios, including $3.80 V$ ($i_{app} = 25$

Table 1

The density and volume fraction of cathode, binding material and separator [8].

| Parameters | Unit | Value |
|-----------------------------|-------------|-------|
| ρ_s (cathode) | $kg m^{-3}$ | 4210 |
| ρ_b (cathode) | $kg m^{-3}$ | 1800 |
| ρ_s (separator) | $kg m^{-3}$ | 855 |
| ρ_e | $kg m^{-3}$ | 1324 |
| ε_s (cathode) | 1 | 0.42 |
| ε_b (cathode) | 1 | 0.10 |
| ε_e (cathode) | 1 | 0.48 |
| ε_s (separator) | 1 | 0.61 |
| ε_e (separator) | 1 | 0.39 |

$A m^{-2}$), $3.70 V$ ($i_{app} = 50 A m^{-2}$) and $3.60 V$ ($i_{app} = 100 A m^{-2}$). The mass of the half cell, m , is calculated by

$$m = A \left(\sum_{i \in cat} \rho_i \varepsilon_i L + \sum_{i \in sep} \rho_i \varepsilon_i L_s \right). \quad (15)$$

In the cathode ("cat") region, the density ρ_i ($kg m^{-3}$) includes the density of active material, ρ_s , the density of the binding material, ρ_b , and the density of electrolyte, ρ_e . ε_i denotes the volume fraction, including the volume fraction of the active material, ε_s , the volume fraction of the binding material, ε_b , and the volume fraction of the electrolyte, ε_e . In the separator region ("sep"), the density ρ_i includes the density of the separator material, ρ_s , and the density of electrolyte, ρ_e . The values of these parameters are given in Table 1. The SOC of a particle is defined by

$$SOC = \frac{c_{s,ave}}{c_{s,max}}. \quad (16)$$

where $c_{s,ave}$ is the average lithium ion concentration in the active material particle.

3. Results and discussions

3.1. Effect of crack semi-axis ratio

In this section, the effect of crack semi-axis ratio, a/b , on cell performance is investigated. The crack angle θ and position d are kept at 0° and $40 \mu m$, respectively. To keep the volume of the active cathode material constant, the crack volume fraction is set to be constant at 3.14% of the total domain. In other words, the area of the ellipse is constant. Therefore, any difference of performance would come purely from the crack geometry, not from any change of the amount of active material. We consider a series of a/b ratios: 20, 12, 6, 2, 0.5, 0.167, 0.083 and 0.05. The corresponding lengths of a and b are calculated based on the ratio and the fixed area of the ellipse. At the ratio of $a/b = 20$ or 0.05, the length of the long semi-axis is $27.7 \mu m$. The direction of a crack is defined by its long axis. For instance, when $a/b = 20$, we say the crack is parallel to the x axis or perpendicular to the current collector. When $a/b = 0.05$, we say the crack is parallel to the y axis or parallel to the current collector. The region inside the crack is first set to be inactive ($W_R=0$) to study the electrolyte dry-out or gas fill-in effects. For simulation, the applied discharge current density, i_{app} , is set to be $25 A m^{-2}$, $50 A m^{-2}$ and $100 A m^{-2}$, respectively. The resulting terminal voltage, specific energy (SE) and specific capacity (SC) curves for various semi-axis ratios are presented in Fig. 2.

Fig. 2a shows that when the crack is parallel to the current collector ($a/b < 1$), the terminal voltage increases significantly with a/b at the same discharge time, especially when i_{app} is large. By contrast, when the crack is perpendicular to the current collector ($a/b > 1$), the terminal voltage curves almost overlap for different a/b values. Fig. 2b and 2c shows that when the crack is parallel

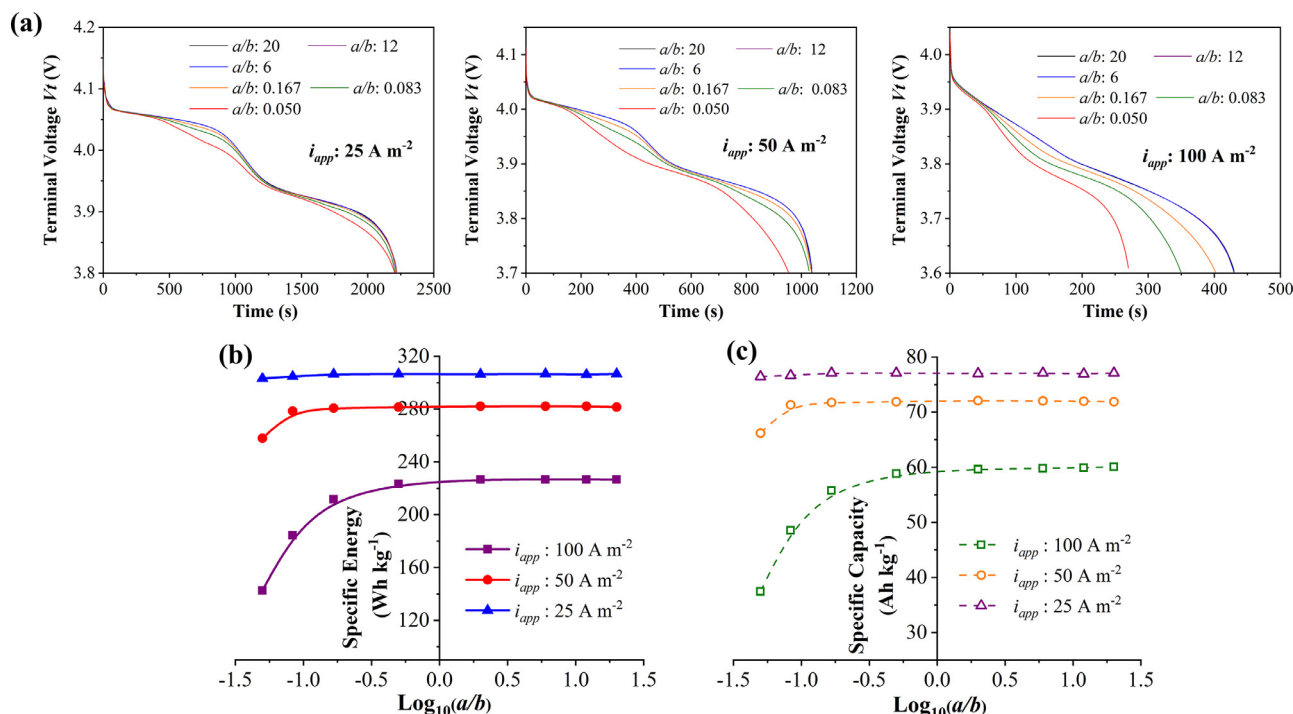


Fig. 2. (a) Terminal voltage curve of a crack-containing cell for various crack semi-axis ratios, a/b , and under various discharge current densities. (b) The specific energy and (c) the specific capacity of a crack-containing cell for various crack semi-axis ratios, a/b , and under various discharge current densities.

to the current collector ($\text{log}_{10}(a/b) < 0$), SE and SC increase significantly with a/b , especially when i_{app} is large. At $i_{app} = 100 \text{ A m}^{-2}$, SE and SC increase by 56.68% and 57.02%, respectively, as a/b increases from 0.05 to 0.167. At a low current density of $i_{app} = 25 \text{ A m}^{-2}$, SE and SC only increase by 1.09% and 0.82%, respectively, as a/b increases from 0.05 to 0.167. When the crack is perpendicular to the current collector ($\text{log}_{10}(a/b) > 0$), SE and SC remain almost constant as a/b increases. These observations suggest that the specific energy and specific capacity of a cell can be significantly affected only when the crack is parallel to the current collector and the discharge current density is large. When the crack is perpendicular to the current collector, the crack geometry (a/b) has little impact. Thus, in experimental analysis, attention should focus more on the cracks parallel to the current collector.

To understand better the above phenomena, we plot the contours of lithium ion concentration in the electrolyte and the local SOC in the cathode under $i_{app} = 50 \text{ A m}^{-2}$ at the instant that the average cathode SOC is 0.50. Fig. 3a shows that with $a/b = 0.05$, the crack significantly blocks Li ion transport from the anode (lithium metal) to the cathode, especially to the region between the crack and the current collector (R-II in Fig. 3a). The average lithium ion concentration in the electrolyte is $1250.0 \text{ mol m}^{-3}$ in region R-I while only 281.1 mol m^{-3} in R-II. The latter is 22.5% of that in R-I. This suggests a severe blocking effect. With $a/b = 0.167$, Li ion transport is less blocked. The average Li ion concentration in the electrolyte is $1060.00 \text{ mol m}^{-3}$ in region R-I and $595.78 \text{ mol m}^{-3}$ in R-II, with the latter being about 56.21% of that in R-I. By contrast, with $a/b = 6$ or 12 , there is almost no blocking effect. The average Li ion concentration in the electrolyte in the whole cathode region is $842.56 \text{ mol m}^{-3}$ ($a/b = 6$) and $842.49 \text{ mol m}^{-3}$ ($a/b = 12$). This suggests that a crack perpendicular to the current collector hardly impedes Li ion transport within the cell.

The local SOC distribution in the cathode material further shows how a crack blocks Li ion transport and affects cathode utilization. Fig. 3b shows that the local SOC is significantly higher in region R-I than in R-II with $a/b = 0.05$ and 0.167 . The reduction re-

action is mostly restricted in R-I during discharging. The discharge capacity will be significantly reduced because of diffusion polarization and significant underuse of region R-II. This effect becomes more significant when the crack is longer and parallel to the current collector. By contrast, the crack hardly distorts the SOC distribution with $a/b = 6$ and 20 . The SOC distribution is more uniform (close to the average cathode SOC of 0.5), indicating a relatively uniform Li ion intercalation. Moreover, the local SOC distribution is almost identical for $a/b = 6$ and 12 .

Next, the effects of applied discharge current density are investigated. The contours of lithium ion concentration in the electrolyte and the local SOC distribution in the cathode material at the instant that the average cathode SOC is 0.5 for $i_{app} = 100 \text{ A m}^{-2}$, 50 A m^{-2} and 25 A m^{-2} are shown in Fig. 4a and 4b.

Fig. 4a shows that the Li ion concentration in the electrolyte becomes more non-uniform with increasing i_{app} . The maximum Li ion concentration in the electrolyte increases from 1567 mol m^{-3} to 2677 mol m^{-3} as i_{app} increases from 25 A m^{-2} to 100 A m^{-2} , while the minimum concentration decreases from 503 mol m^{-3} to 39 mol m^{-3} . Besides, the difference of average electrolyte Li ion concentration in regions R-I and R-II increases from $631.52 \text{ mol m}^{-3}$ to $1113.52 \text{ mol m}^{-3}$ as i_{app} increases from 25 A m^{-2} to 100 A m^{-2} , as shown in Fig. 4c. This phenomenon indicates a stronger blocking effect of Li ion transport by the crack under larger discharge current densities. When i_{app} is large (e.g. 100 A m^{-2}), a larger amount of Li ions move from the lithium metal surface to region R-I in a unit time. Because of the narrow passage between the crack tip and the boundary, more Li ions are trapped in R-I. When i_{app} is small, a smaller amount of Li ions move to R-I in a unit time, so that a larger portion of those ions can pass through the narrow passage to R-II. Then the concentration difference between R-I and R-II is smaller. Similarly, as shown in Fig. 4b, the average local cathode SOC is larger in R-I than in R-II and this difference increases with the discharge current density. Fig. 4c shows that the difference is 0.12 under $i_{app} = 25 \text{ A m}^{-2}$ but increases to 0.28 under $i_{app} = 100 \text{ A m}^{-2}$.

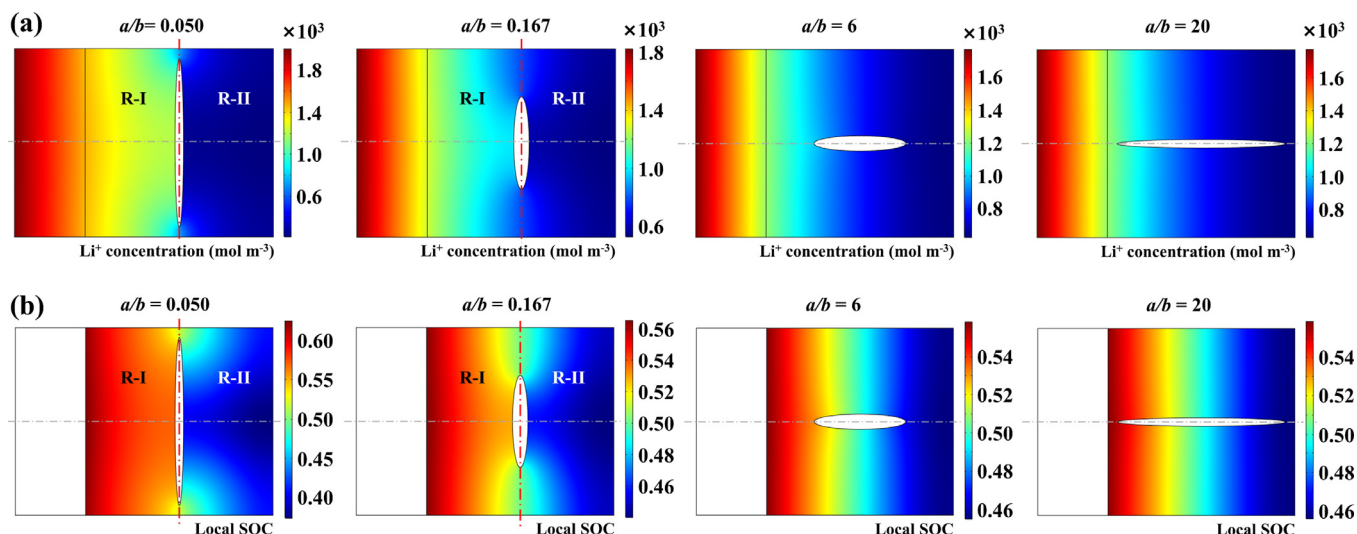


Fig. 3. (a) The contours of lithium ion concentration in the electrolyte in a crack-containing cell for various crack a/b ratios. (b) The contours of local SOC in the cathode for various crack a/b ratios. (i_{app} : 50 A m^{-2} , average cathode SOC: 0.5, W_R : 0).

A crack may sometimes contain different amounts of electrolyte in the form of absorbed electrolytes on the inner surface of the crack. This calls for a study of cell performance with different wetting ratios on the crack surface. Cracks with $a/b = 0.05, 0.083, 0.167$, and $W_R = 0, 0.2, 0.4, 0.6$ and 1.0 are considered. The geometrical characteristic of the electrolyte-wetted crack is shown in Fig. 1b. The specific energy under $i_{app} = 50$ A m^{-2} is calculated and shown in Fig. 5. The wetting electrolyte (described by W_R) on crack surfaces increases the total cell mass, and this total mass is used to calculate the specific energy. So for specific energy, the additional mass associated with the wetting electrolyte is accounted for. In addition to the specific energy, we also show the cell energy to directly compare the effect of wetting ratio (the cell with a larger W_R has a slightly larger mass).

Fig. 5a shows that the cell energy increases rapidly with W_R from 0 to 0.4, especially for the crack with $a/b = 0.05$. When W_R further increases from 0.4 to 1.0, the cell energy only increases slightly, indicating that an increase of the wetting ratio has less effect on cell performance when W_R is larger. Besides, with $W_R = 1.0$, the cell energy appears to converge to a similar value for various a/b . This can be understood by analyzing the Li ion concentration in the electrolyte and local SOC distribution. Fig. 5b and 5c shows the contours for $a/b = 0.05$. As can be seen in Fig. 5b, the blockage of Li ion transport is reduced with increasing W_R . When $W_R = 1.0$, Li ions can almost completely pass through the crack. Therefore, a larger W_R reduces the diffusion polarization due to the existence of a crack, leading to an increased energy. Since a crack filled with electrolyte is different from a crack filled with active material (i.e. no crack), the crack geometry still has a slight impact. The cell energy with $a/b = 0.167$ is slightly larger than that with $a/b = 0.05$ at $W_R = 1.0$. Comparing to the cell energy, the specific energy shows a different dependence on W_R . The SE initially increases to a peak value and then decreases with W_R , as shown in Fig. 5a, especially for the cell with $a/b = 0.05$. This phenomenon is a result of more system mass from the increasing wetting ratio.

The effect of crack geometrical characteristics on cell performance is further quantified in terms of EIS simulations at 0.5 cathode SOC. The Nyquist plots of impedance are shown in Fig. 6.

Fig. 6a shows a left shift, or a reduction of ohmic resistance, with a/b . The reduction is significant when a/b increases from 0.05 to 0.167, but does not change much when a/b increases from 6 to 20. This behavior is consistent with the blocking of Li ion transport shown in Fig. 3, where a crack parallel to the current col-

lector has a larger blocking effect. The radius of the semi-circle does not change much with a/b , indicating no impact on charge transfer resistance. These suggest that the major impact by a crack is an increase of the electrolyte resistance. A comparison of the impedance spectrum between cells with ($a/b = 20$) and without a crack in Fig. 6b shows that they almost overlap with each other, indicating that a crack perpendicular to the current collector has little impact on cell impedance. Fig. 6c shows that a larger crack wetting ratio slightly reduces the ohmic resistance as a result of increasing ion transport with W_R . Fig. 6d shows that the effect of wetting ratio is stronger on a more elongated crack parallel to the current collector.

3.2. Effect of crack angle

In this section we investigate the impact of crack angle, θ , on cell performance. Five angles of $0^\circ, 30^\circ, 45^\circ, 60^\circ$ and 90° are selected with a/b being 20, 12 and 6. Because of $a/b > 1$, the crack is perpendicular to the current collector with $\theta = 0^\circ$ and parallel to the current collector with $\theta = 90^\circ$. The crack position d is kept at 40 μm . Fig. 7 shows the calculated specific energy and specific capacity under $i_{app} = 50$ A m^{-2} and 100 A m^{-2} .

With $i_{app} = 50$ A m^{-2} , the SE and SC decrease slightly when θ increases from 0° to 45° , but decrease rapidly when θ increases from 45° to 90° , as shown in Fig. 7a and 7b. The reduction of SE and SC from 0° to 90° is 9.33% and 12.76%, respectively for a longer crack of $a/b=20$. For a shorter crack having a smaller a/b (e.g. $a/b=12$ and 6), the impact of crack angle is smaller. However, at a higher current density of $i_{app} = 100$ A m^{-2} , all cracks are significantly affected by the angle as shown in Fig. 7c and 7d. For a longer crack of $a/b=20$ at this current density, the SE and SC decrease at approximately constant rates, 0.932 Wh kg^{-1} degree $^{-1}$ and 0.246 Ah kg^{-1} degree $^{-1}$, respectively. The reduction of SE and SC from 0° to 90° is 37.06% and 37.42% respectively. These are much larger than those with $i_{app} = 50$ A m^{-2} . These observations suggest that low discharge current densities and long cracks tend to cause a non-linear decrease of SE and SC with increasing crack angle. When the discharge current density is high or the crack is short, the decrease of SE and SC is roughly linear with the crack angle.

The Li ion concentration in the electrolyte and the local SOC in the cathode at the instant that the average cathode SOC is 0.50 are shown in Fig. 8. The blocking of Li ion transport is significantly dependent on the crack angles, as shown in Fig. 8a. The Li ion con-

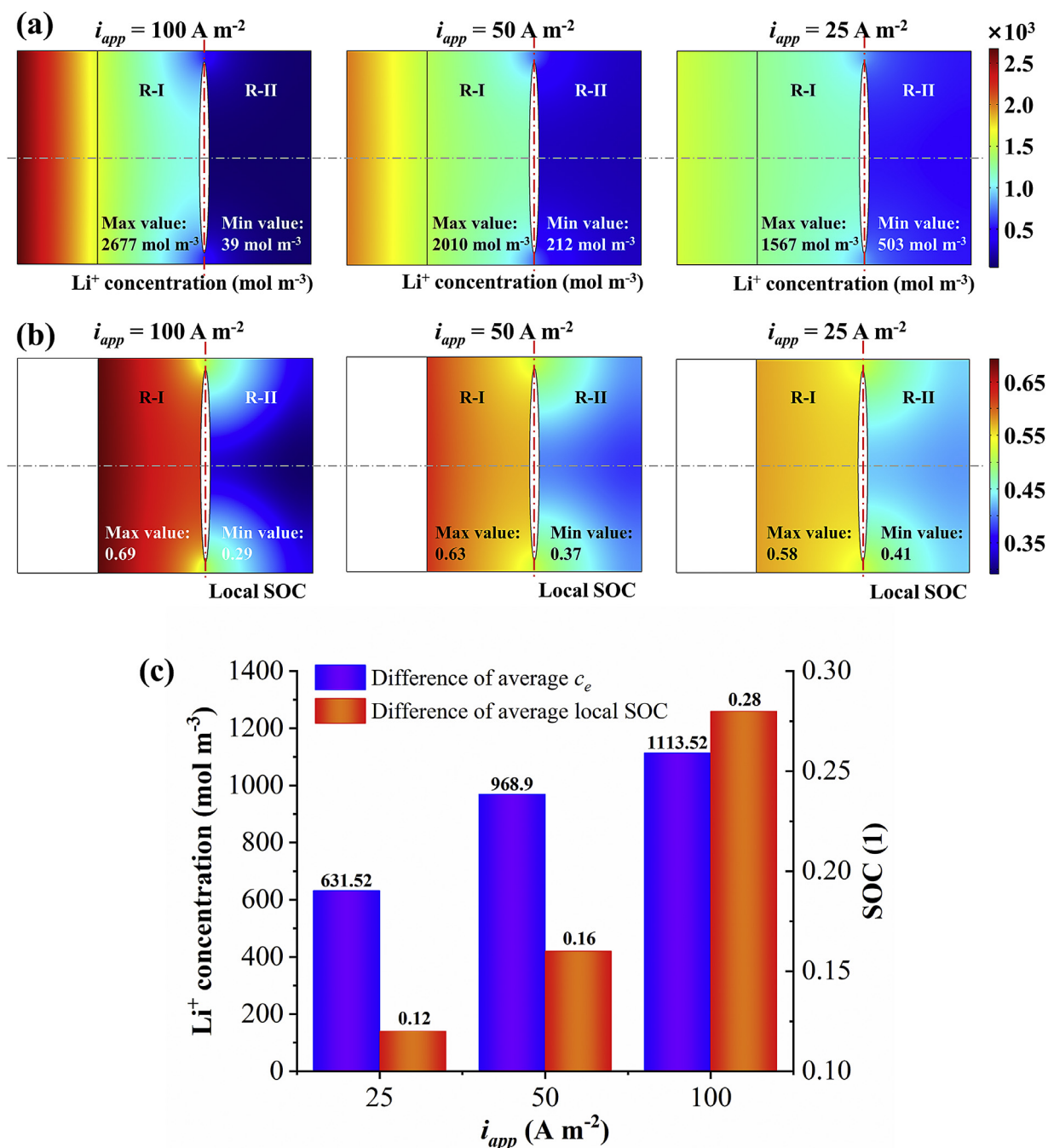


Fig. 4. (a) The contours of lithium ion concentration in the electrolyte under various discharge current densities (a/b : 0.05, average cathode SOC: 0.5). (b) The contours of local SOC in the cathode under various discharge current densities (a/b : 0.05, average cathode SOC: 0.5). (c) The difference of average lithium ion concentration in the electrolyte and average local SOC in the cathode between regions R-I and R-II (a/b : 0.05, average cathode SOC: 0.5).

centration in region A-I is larger than that in A-II. At $\theta = 30^\circ$, the average concentration is 1020 mol m^{-3} in A-I and $631.57 \text{ mol m}^{-3}$ in A-II, a difference of $388.43 \text{ mol m}^{-3}$. At $\theta = 45^\circ$, the average concentration is 1100 mol m^{-3} in A-I and $518.42 \text{ mol m}^{-3}$ in A-II, a difference of $581.58 \text{ mol m}^{-3}$. The difference becomes more significant. At $\theta = 60^\circ$, the average concentration becomes 1170 mol m^{-3} in A-I and $402.17 \text{ mol m}^{-3}$ in A-II, a difference of $767.83 \text{ mol m}^{-3}$. The difference is 968.9 mol m^{-3} at $\theta = 90^\circ$ (see Fig. 3a with $a/b = 0.05$). Considering the blocking effect, a long crack can be approximately projected into two components: one along the x axis (perpendicular to the current collector) and one along the y axis (parallel to the current collector), as indicated by the green dash

lines in Fig. 8a. The component parallel to the current collector has a major impact in blocking Li ion transport, while the component perpendicular to the current collector has almost no effect. Therefore, for a system composed of multiple cracks and crack angles, the sum of projected crack length parallel to the current collector is an indicator to roughly but quickly indicate the significance of cracks in blocking Li ion transport. This could be handy when comparing samples experimentally.

Fig. 8b shows that the local cathode SOC is larger in region A-I than that in A-II, a trend similar to Fig. 8a. The difference of average SOC in A-I and A-II (separated by the dash line along the crack) increases with the crack angle. This increase is 0.02 as the

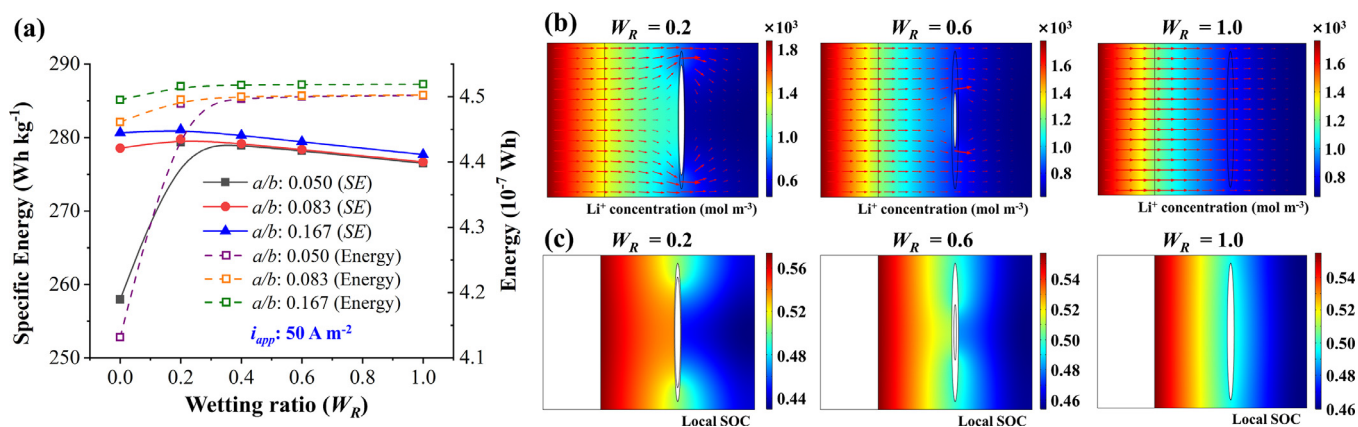


Fig. 5. (a) The energy and specific energy of a crack-containing cell for various crack wetting ratios. (b) The contours of lithium ion concentration in the electrolyte for various crack wetting ratios (a/b : 0.05, average cathode SOC: 0.5). (c) The contours of local SOC in the cathode for various crack wetting ratios (a/b : 0.05, average cathode SOC: 0.5). Shown for discharge current at $i_{app} = 50 \text{ A m}^{-2}$.

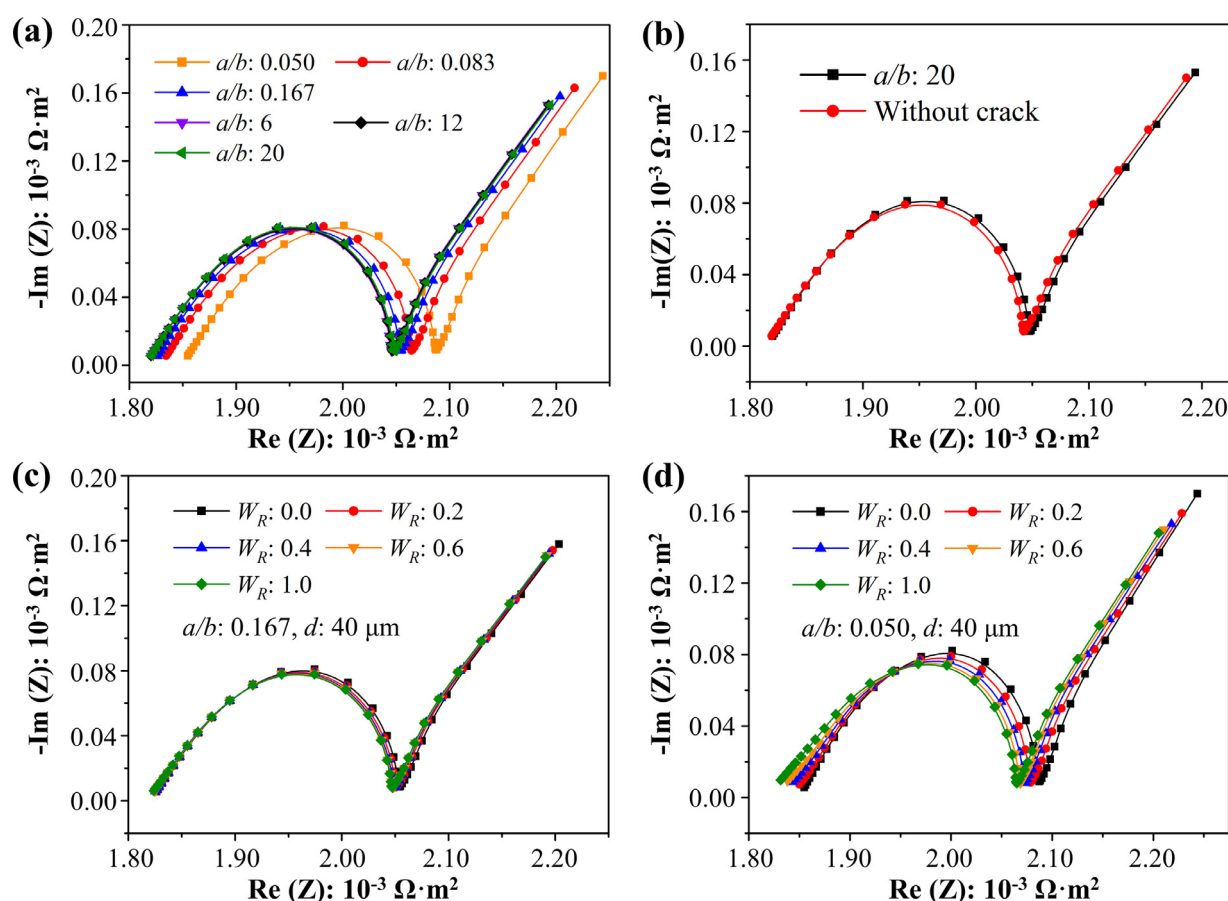


Fig. 6. (a) The impedance spectrum of a crack-containing cell for various crack semi-axis ratios (W_R : 0). (b) A comparison of the impedance spectrum between cells with and without a crack (W_R : 0). (c) The impedance spectrum for various crack wetting ratios with $a/b = 0.167$. (d) The impedance spectrum for various crack wetting ratios with $a/b = 0.05$.

crack angle increases from 30° to 45°, and 0.03 as the angle increases from 45° to 60°.

The added effect of crack wetting ratios with W_R being 0.0, 0.2, 0.4, 0.6 and 1.0 are considered in Fig. 9. It is seen that the cell energy increases with W_R . The increase is more significant with $a/b = 20$ than that with $a/b = 6$. When the crack is totally filled with electrolyte ($W_R = 1$), the curves of different crack angles converges to the same point. With $a/b = 20$, the SE initially increases to a peak and then decreases with W_R , especially for $\theta = 60^\circ$. With $a/b = 6$, the SE decreases monotonously with W_R . These

phenomena are caused by the increased mass from the wetting electrolyte.

The EIS analysis is conducted to investigate the relationship between the crack angle and the cell impedance. The a/b ratios are set to be 20, 12 and 6. The SOC of cathode particles is set to be 0.5. Fig. 10a–c shows that as the crack angle increases, the ohmic resistance increases slightly. The increase is more significant for a longer crack with $a/b = 20$, as shown in Fig. 10c. This is consistent with the previous observation that the Li ion blocking effect is stronger when the crack is more parallel to the current collec-

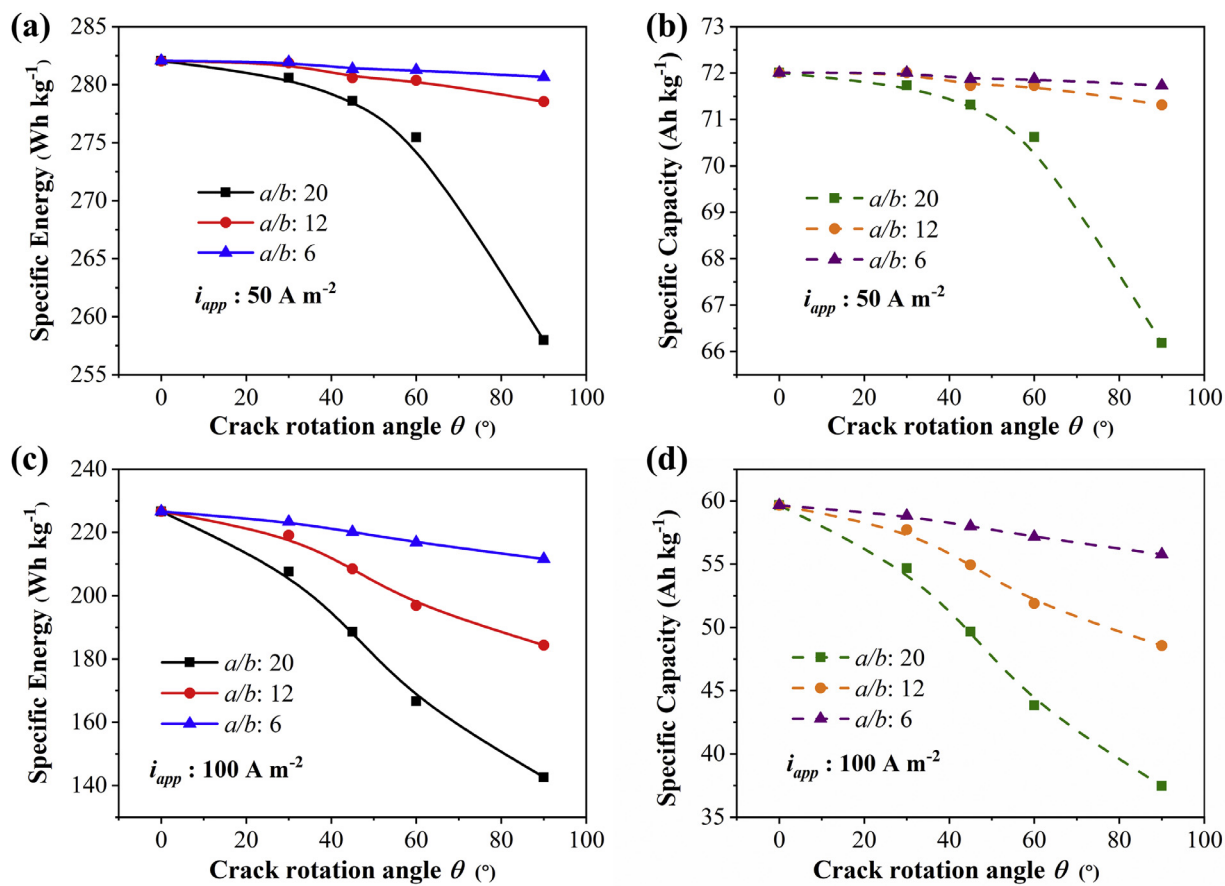


Fig. 7. (a) The specific energy of a crack-containing cell for various crack angles with $i_{app} = 50$ A m⁻². (b) The specific capacity of a crack-containing cell for various crack angles with $i_{app} = 50$ A m⁻². (c) The specific energy of a crack-containing cell for various crack angles with $i_{app} = 100$ A m⁻². (d) The specific capacity of a crack-containing cell for various crack angles with $i_{app} = 100$ A m⁻².

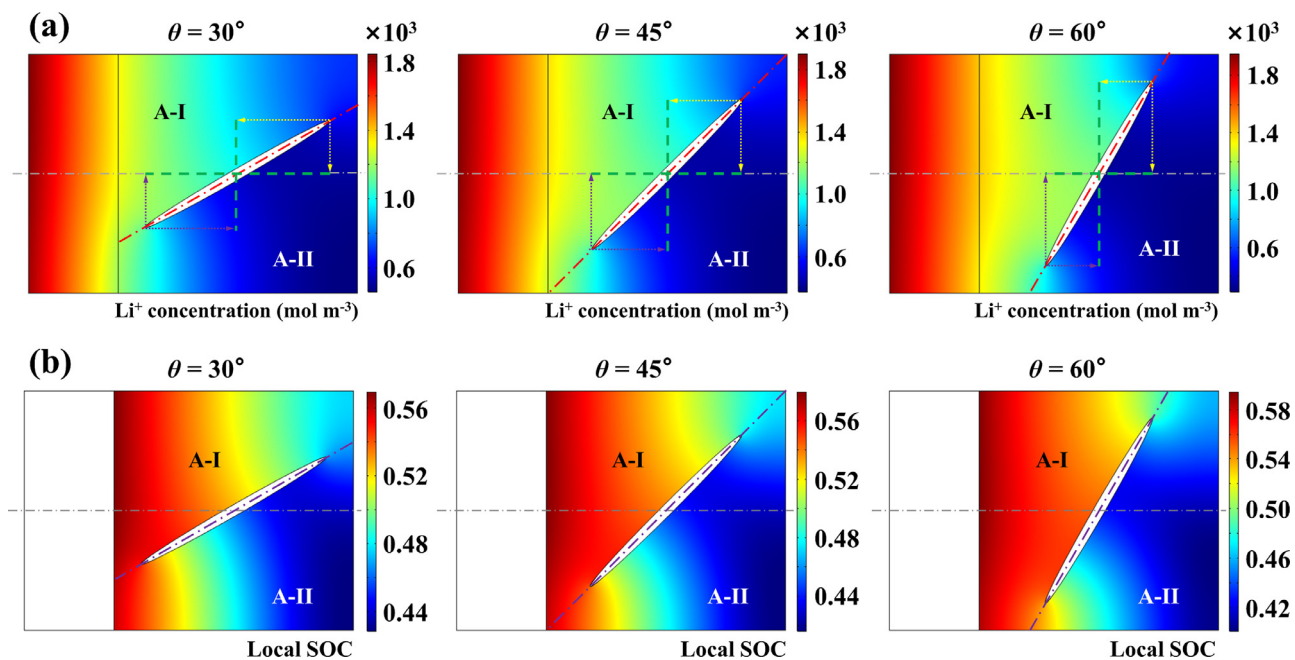


Fig. 8. (a) The contours of lithium ion concentration in the electrolyte for various crack angles. (b) The contours of local SOC in the cathode for various crack angles. ($i_{app} = 50$ A m⁻², $a/b = 20$, average cathode SOC: 0.5, $W_R = 0$).

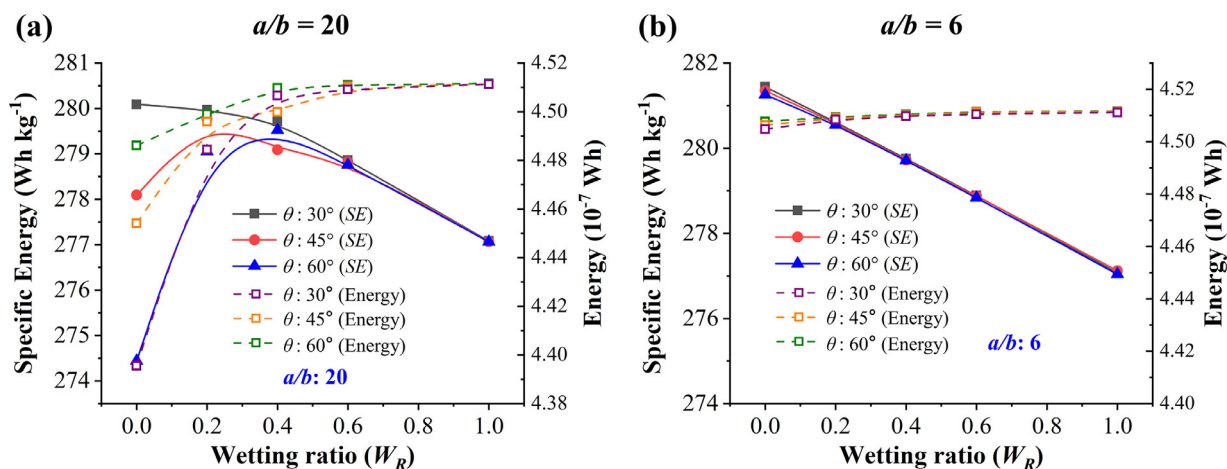


Fig. 9. The energy and specific energy of a crack-containing cell for various crack wetting ratios. (a) $a/b = 20$. (b) $a/b = 6$. (i_{app} : 50 A m^{-2} , cathode average SOC: 0.5).

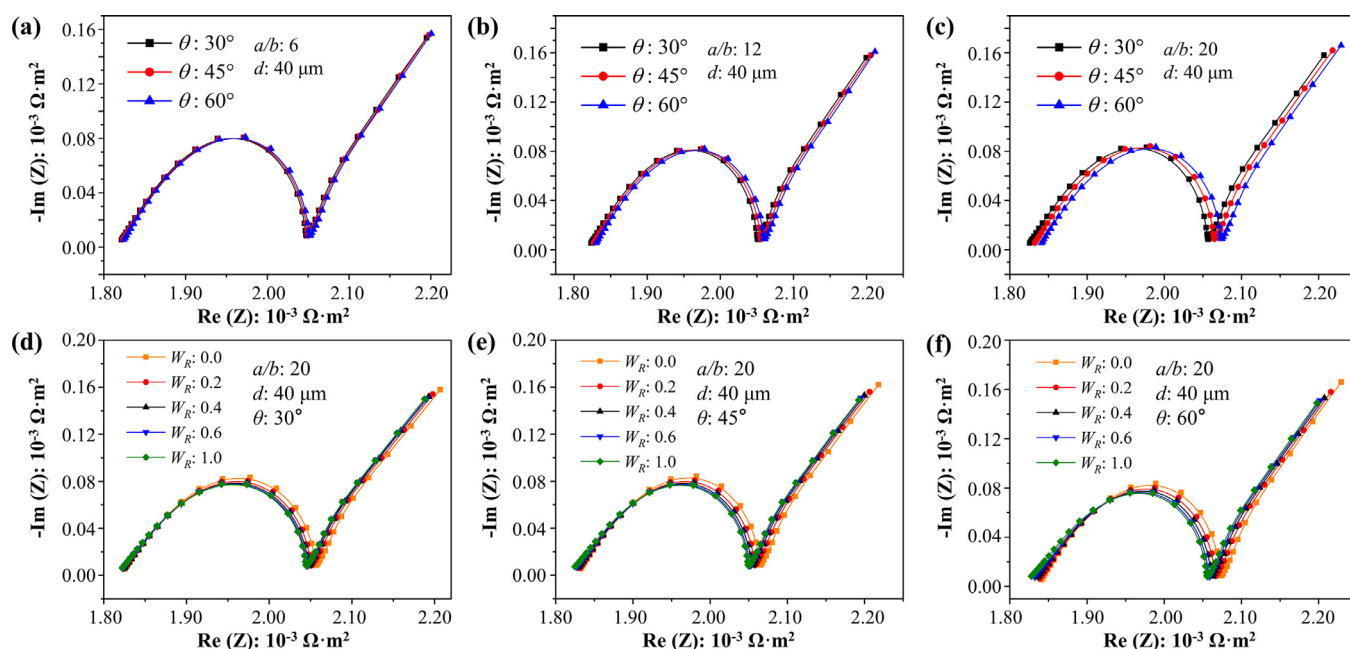


Fig. 10. (a–c) The impedance spectrum of a crack-containing cell for various crack angles and semi-axis ratios (W_R : 0, average cathode SOC: 0.5). (a) $a/b = 6$. (b) $a/b = 12$. (c) $a/b = 20$. (d–f) The impedance spectrum of a crack-containing cell for various crack angles and crack wetting ratios (a/b : 20, average cathode SOC: 0.5). (d) $\theta = 30^\circ$. (e) $\theta = 45^\circ$. (f) $\theta = 60^\circ$.

tor and when the crack is longer. From Fig. 10d–f, it is seen that the ohmic resistance decreases with the wetting ratio. The effect is more significant for a larger angle, as seen in Fig. 10f. This is because Li ion blocking is stronger for a larger crack angle, so that the help from crack wetting is more effective.

3.3. Effect of crack position

In this section, the crack central position is taken into consideration. The d values are selected to be $10 \mu\text{m}$, $25 \mu\text{m}$, $40 \mu\text{m}$, $55 \mu\text{m}$ and $70 \mu\text{m}$ with a/b being 0.05, 0.083 and 0.167, and i_{app} being 50 A m^{-2} and 100 A m^{-2} . The angle is fixed at $\theta = 0^\circ$, so that $a/b < 1$ represents a crack parallel to the current collector. The crack with $a/b = 0.05$ is the longest crack among the three. After simulations, the specific energy and specific capacity are presented in Fig. 11. It can be seen that the SE and SC increase dramatically with d . For instance, with $i_{app} = 100 \text{ A m}^{-2}$ and $a/b = 0.05$, the

SE (Fig. 11c) and SC (Fig. 11d) increase by 282.45% and 276.14%, respectively, as d increases from $10 \mu\text{m}$ to $70 \mu\text{m}$. For $a/b = 0.083$, the increase is 68.10% and 67.72% respectively. This suggests that a long parallel crack close to the separator significantly reduces the specific energy and specific capacity. When the crack is closer to the current collector, the impact is smaller, and the crack shape also seems insignificant since all curves converge to the same point with increasing d for various a/b ratios. The effect of crack position becomes increasingly significant when the discharge current density is higher.

To further understand the phenomena, the Li ion concentration in the electrolyte and the local SOC distribution in the cathode are presented in Fig. 12. It can be seen from Fig. 12a that the Li ion concentration becomes increasingly non-uniform with decreasing d , i.e. when the crack is closer to the separator. At $d = 10 \mu\text{m}$, the average Li ion concentration in region D-II is $437.79 \text{ mol m}^{-3}$, which is only 22.8% of that in D-I (1920 mol m^{-3}). The crack significantly blocks Li ion transport, restricting the reaction to occur

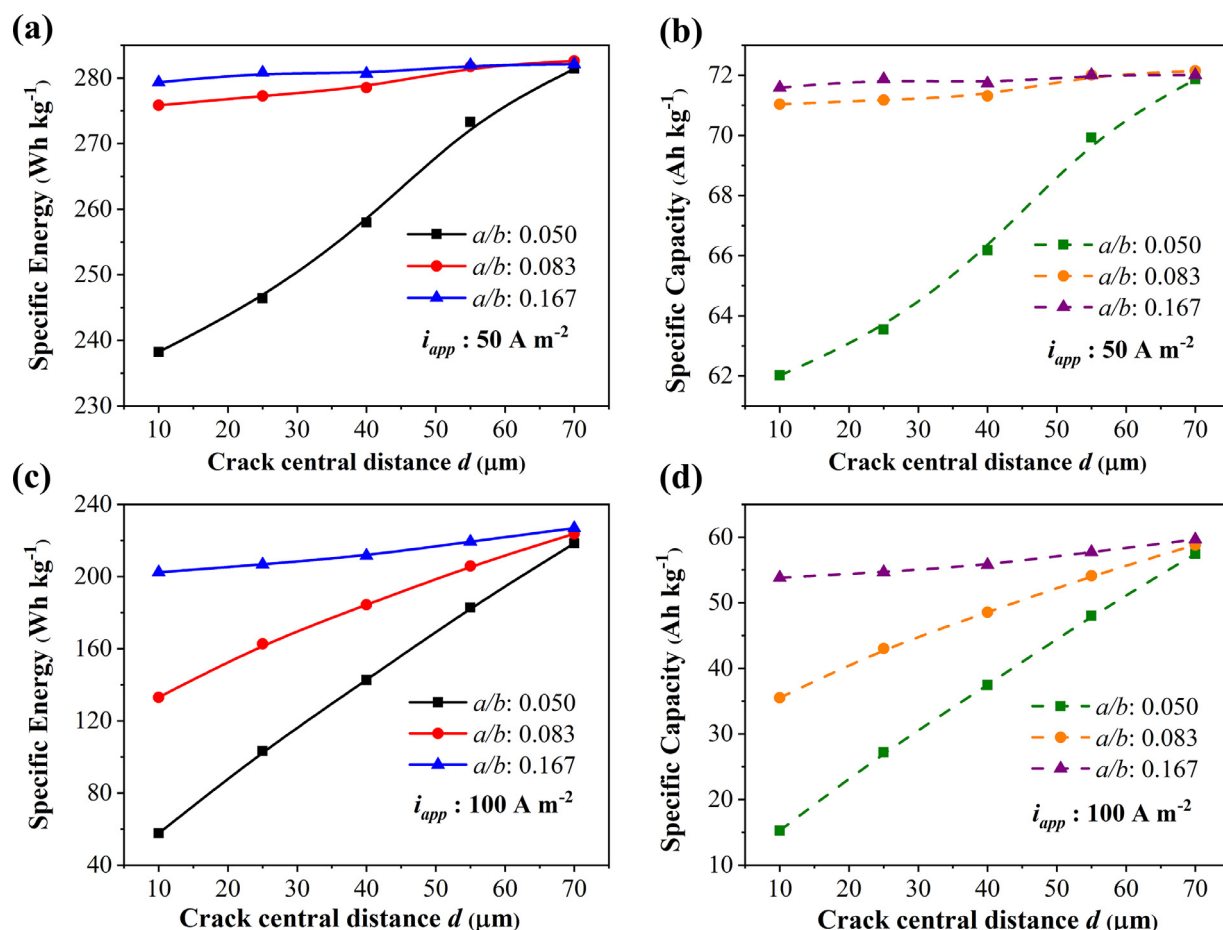


Fig. 11. (a) The specific energy of a crack-containing cell for various crack positions with $i_{app} = 50 \text{ A m}^{-2}$. (b) The specific capacity of a crack-containing cell for various crack positions with $i_{app} = 50 \text{ A m}^{-2}$. (c) The specific energy of a crack-containing cell for various crack positions with $i_{app} = 100 \text{ A m}^{-2}$. (d) The specific capacity of a crack-containing cell for various crack positions with $i_{app} = 100 \text{ A m}^{-2}$. The crack is parallel to the current collector since $a/b < 1$.

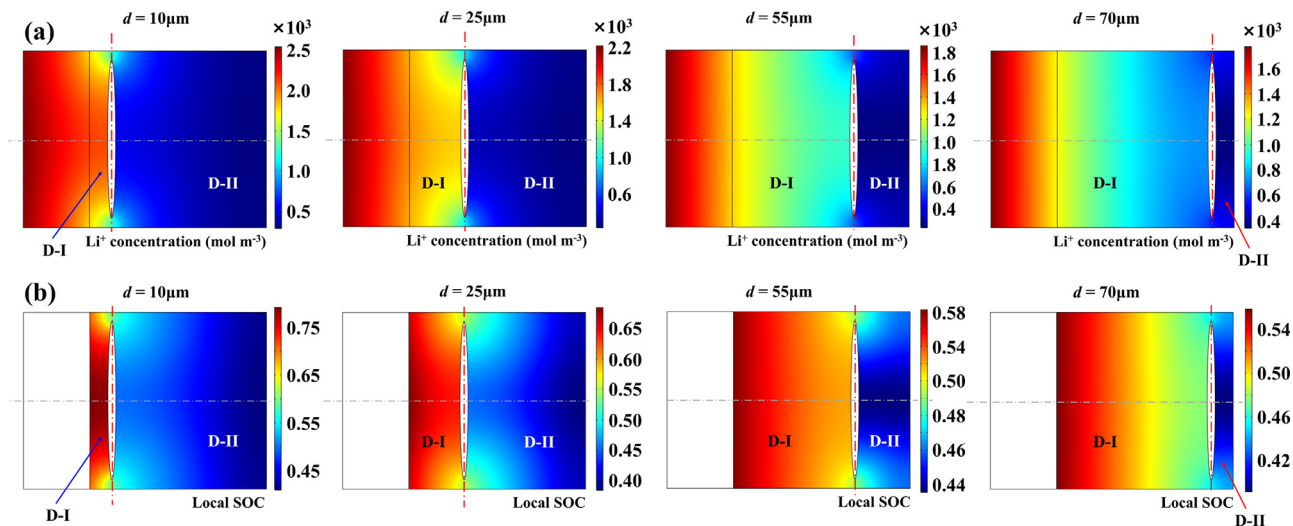


Fig. 12. (a) The contours of lithium ion concentration in the electrolyte in a crack-containing cell for various crack positions. (b) The contours of local SOC in the cathode for various crack positions. ($i_{app} = 50 \text{ A m}^{-2}$, average cathode SOC: 0.5, $W_R = 0$, $a/b = 0.05$).

mostly in a small region D-I. With increasing d , the Li ion concentration in D-I decreases significantly, and the difference of average concentration between the left and the right of the crack also decreases significantly. At $d = 70 \mu\text{m}$, the average Li ion concentration in D-II ($413.99 \text{ mol m}^{-3}$) increases to 46.2% of that in D-I

($895.45 \text{ mol m}^{-3}$). From Fig. 12b, the average local SOC in D-I is 0.74 at $d = 10 \mu\text{m}$, which is significantly larger than that in D-II (0.47) and the difference is 0.27. As d increases, the difference becomes smaller. For instance, the difference reduces to 0.09 when $d = 70 \mu\text{m}$. Fig. 12 shows that when a crack is closer to the sep-

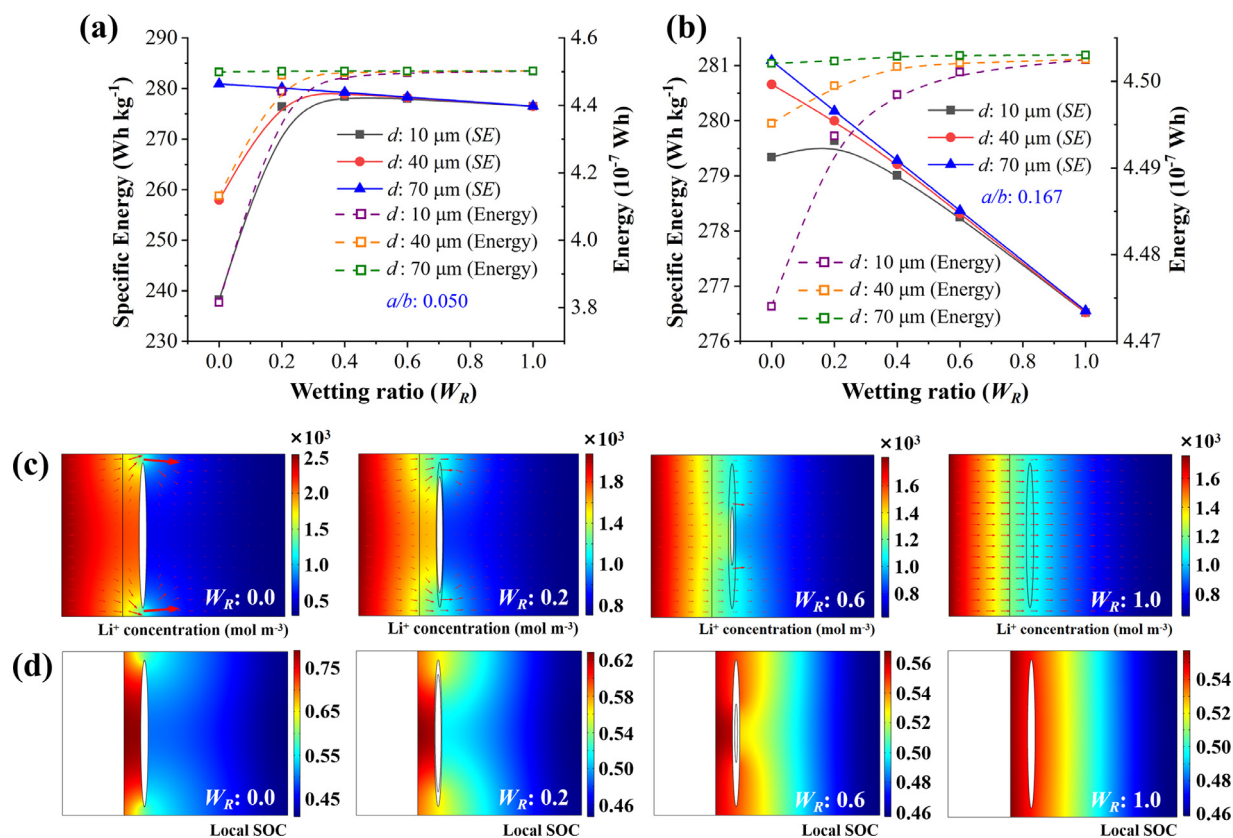


Fig. 13. (a) The energy and specific energy of a crack-containing cell for various crack positions (a/b : 0.05, i_{app} : 50 A m⁻²). (b) The energy and specific energy of a crack-containing cell for various crack positions (a/b : 0.167, i_{app} : 50 A m⁻²). (c) The contours of lithium ion concentration in the electrolyte in a crack-containing cell for various wetting ratios (a/b : 0.05, d : 10 μ m, i_{app} : 50 A m⁻², average cathode SOC: 0.5). (d) The contours of local SOC in the cathode for various wetting ratios (a/b : 0.05, d : 10 μ m, i_{app} : 50 A m⁻², average cathode SOC: 0.5).

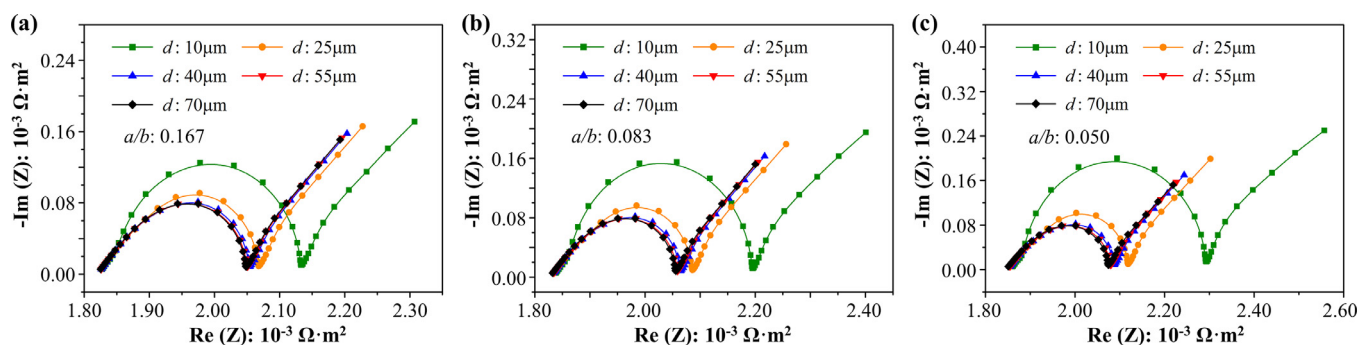


Fig. 14. The impedance spectrum of a crack-containing cell for various crack positions. (a) $a/b = 0.167$. (b) $a/b = 0.083$. (c) $a/b = 0.05$. (average cathode SOC: 0.5).

arator, more cathode material between the crack and the current collector is underuse, leading to a significant decrease of specific energy and specific capacity.

We further consider the wetting ratios $W_R = 0.0, 0.2, 0.4, 0.6, 1.0$ with $i_{app} = 50$ A m⁻². The results are plotted in Fig. 13. For $a/b = 0.05$ and $d = 10$ μ m, the cell energy increases rapidly with W_R (Fig. 13a). The energy also increases with W_R for $d = 40$ μ m and 70 μ m, but the effect is not as significant. The SE either first increases with W_R and then decreases, or decreases monotonously, because of the increasing system mass by crack wetting. These trends appear similar for $a/b = 0.05$ in Fig. 13b. Fig. 13c and 13d shows that increasing wetting reduces Li ion blocking and makes the concentration more uniform. This crack wetting is especially beneficial when the crack is close to the separator. Fig. 13c and 13d shows that with $W_R = 1$, Li ions can completely pass through the crack as if the crack does not exist.

Fig. 14 shows the results of EIS analysis for $d = 10$ μ m, 25 μ m, 40 μ m, 55 μ m and 70 μ m. The a/b ratios are set to be 0.050, 0.083 and 0.167. The cathode SOC is set to be 0.5. It can be observed that the radius of the semi-circle increases dramatically as d is reduced, especially with $a/b = 0.05$. This indicates that the charge transfer resistance increases dramatically as the crack is closer to the separator. This can be understood in terms of the Li blocking effect. It is known that the electrode material next to the separator is more contributive in the electrochemical reaction. When a crack is closer to the separator, the more contributive material is excluded from the reaction, leading to an increased charge transfer resistance. The effect is stronger when the crack is closer to the separator. When d is large ($d \geq 55$ μ m), most of the cathode can participate in the reaction, so that the charge transfer resistance is significantly reduced. Interestingly, the ohmic resistance (electrolyte resistance) does not show any noticeable change with d . This is because re-

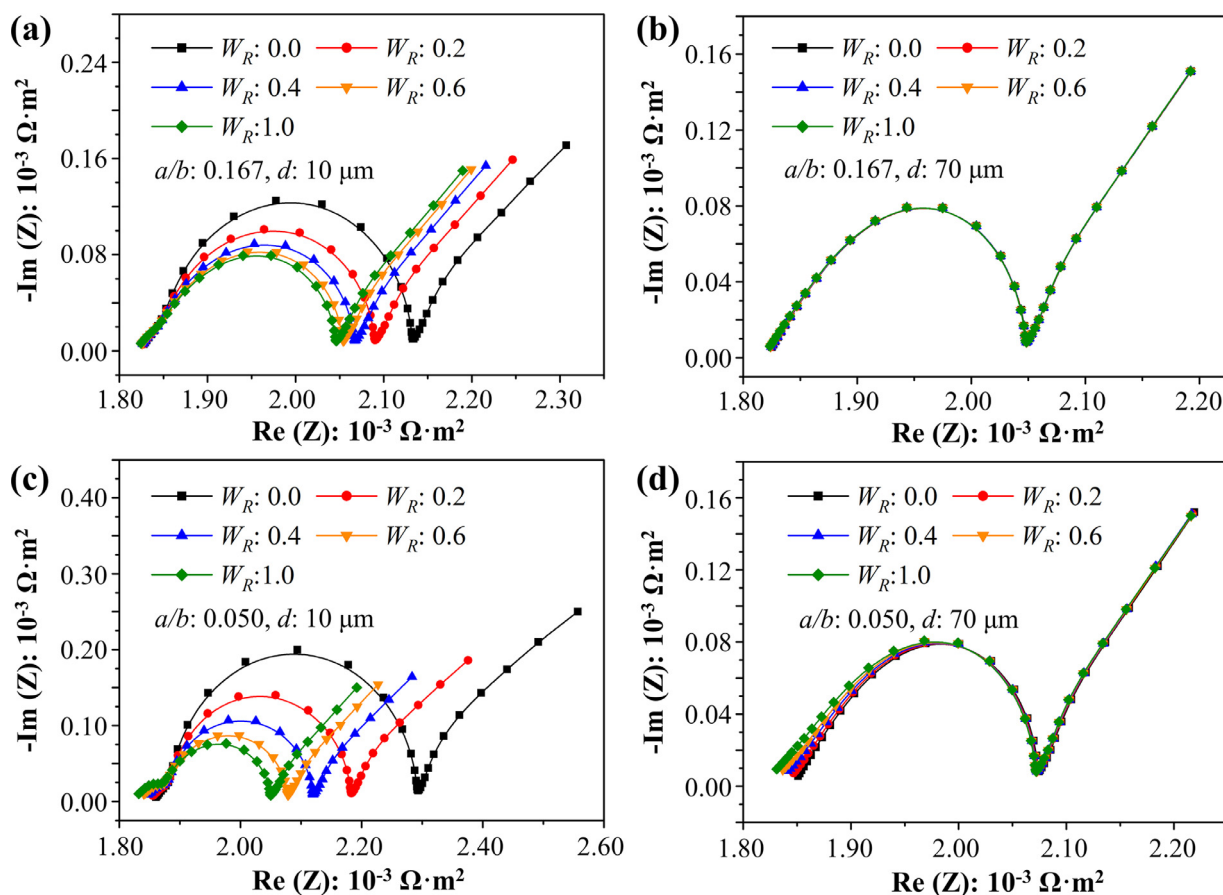


Fig. 15. The impedance spectrum of a crack-containing cell for various wetting ratios. (a) $d = 10 \mu\text{m}$, $a/b = 0.167$. (b) $d = 70 \mu\text{m}$, $a/b = 0.167$. (c) $d = 10 \mu\text{m}$, $a/b = 0.05$. (d) $d = 70 \mu\text{m}$, $a/b = 0.05$. (cathode average SOC: 0.5).

regardless of the crack position, Li ions need to diffuse around the crack in a similar way. Therefore, the ohmic resistance does not show any dependence on the crack position. By contrast, the crack geometry and crack angle affect how Li ions diffuse around the crack, and therefore affect the ohmic resistance.

Fig. 15 shows the effect of wetting ratio with W_R being 0.0, 0.2, 0.4, 0.6 and 1.0. At $d = 10 \mu\text{m}$ (Fig. 15a and 15c), the radius of the semi-circle decreases significantly with W_R , indicating a strong decrease of the charge transfer resistance with the wetting ratio. The increased Li ion transport through the electrolyte adhered to the crack inner wall allows kinetic reaction to occur in a large part of the cathode region. By contrast, at $d = 70 \mu\text{m}$ (Fig. 15b and 15d), the radius of the semi-circle remains unchanged with W_R . The ohmic resistance remains unchanged with W_R at $a/b = 0.167$ (Fig. 15a and 15b). However, at $a/b = 0.05$, the ohmic resistance also shows a reduction with W_R because the crack is longer and has a stronger blocking effect, so that the help from electrolyte wetting is more effective.

4. Closed crack and material isolation

In previous sections we consider a straight crack. In an actual Li-ion cell, the crack shape can be complicated. Sometimes several cracks can connect into a ring shape and isolate an island of active material. Here we consider a ring-shaped crack with different opening sizes and directions (Fig. 16a). The crack opening size is characterized by the angle β . The opening direction is described by the angle α . The crack outer radius, R_{out} , remains constant at $25 \mu\text{m}$. In order to ensure a constant crack area (taken to be 1.9625% of the total cathode area), the inner radius of the crack, R_{in} , is cal-

culated based on the crack opening β . Three α values (0° , 90° , 180°) and seven β values (0° , 11.25° , 22.5° , 45° , 67.5° , 90° , 135°) are considered. The other cell geometrical parameters are the same as those used in previous sections. The applied discharge current density is 50 A m^{-2} . After simulations, the specific energy and specific capacity are calculated and presented in Fig. 16b and 16c.

With $\alpha = 0^\circ$, the SE is almost a constant when β decreases from 135° to 22.5° (Fig. 16b), but decreases sharply as β decreases from 22.5° to 0° . The SC curve shows a similar trend (Fig. 16c). These suggest that for a ring-shaped crack with the opening toward the separator, the cell performance is only significantly affected when the crack is almost closed. By contrast, with $\alpha = 180^\circ$ or the crack opening toward the current collector, the SE decreases gradually as β is reduced from 135° to 22.5° . The SC curve shows a similar trend. For a crack with $\alpha = 90^\circ$, the cell performance lies in between $\alpha = 0^\circ$ and 180° .

To further understand the phenomena, the Li ion concentration in the electrolyte and the local SOC distribution in the cathode are presented in Fig. 17. It is seen that the electrolyte Li ion concentration inside the region enclosed by the crack changes significantly with the crack opening direction. When the crack opening direction is toward the separator ($a = 0^\circ$), Li ion can diffuse into the region enclosed by the crack (region B-II), so that the material can contribute to energy storage. Fig. 17b for $a = 0^\circ$ shows a high SOC inside the enclosed region. When the crack opening direction is toward the current collector ($a = 180^\circ$), Li ions can hardly diffuse inside the enclosed region (see B-II in Fig. 17a for $a = 180^\circ$). Correspondingly, the SOC inside the enclosed region is low (see B-II in Fig. 17b for $a = 180^\circ$). With $a = 90^\circ$, Li ions can partially diffuse into the enclosed region through the crack opening, causing

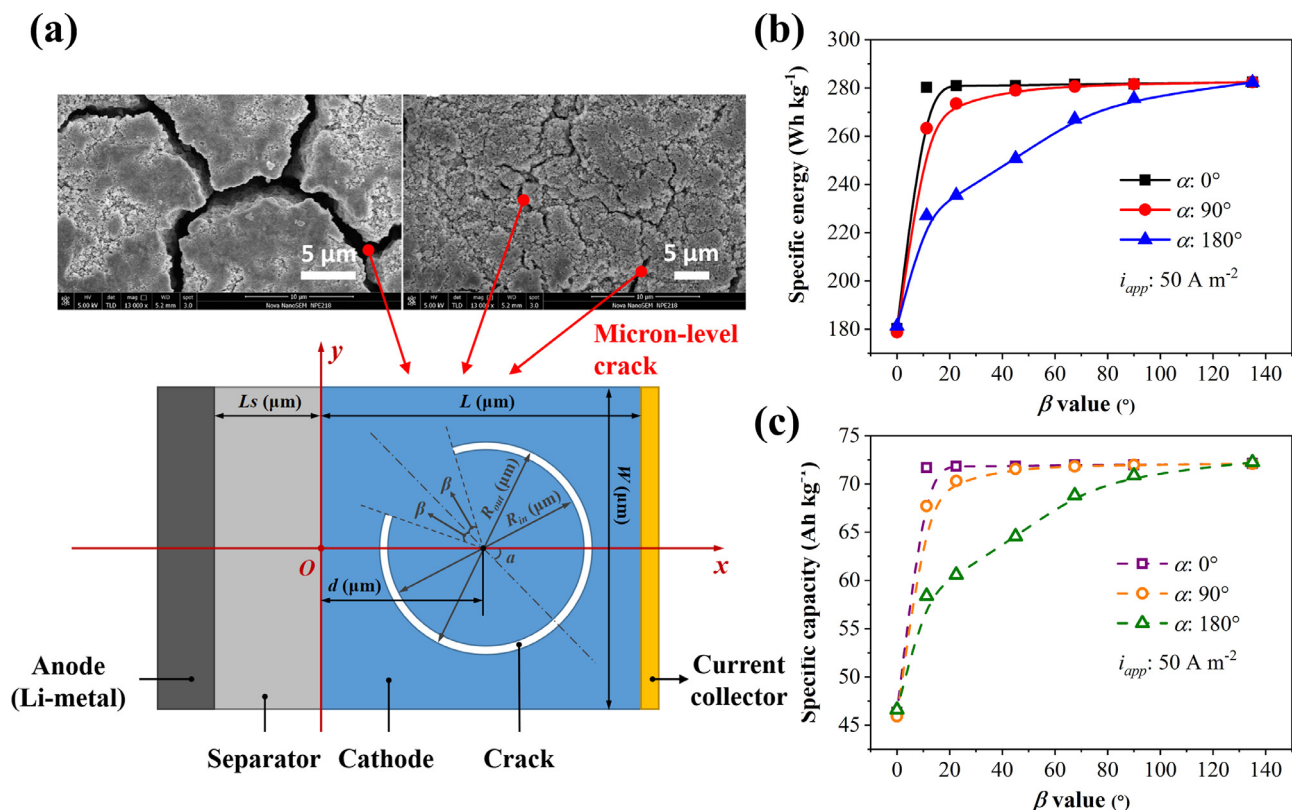


Fig. 16. (a) The setup of a ring-shaped crack in the electrode. The SEM images are reprinted from Bie et al. [31] with permission from Elsevier. (b) The specific energy and (c) specific capacity of the cell with a ring-shaped crack.

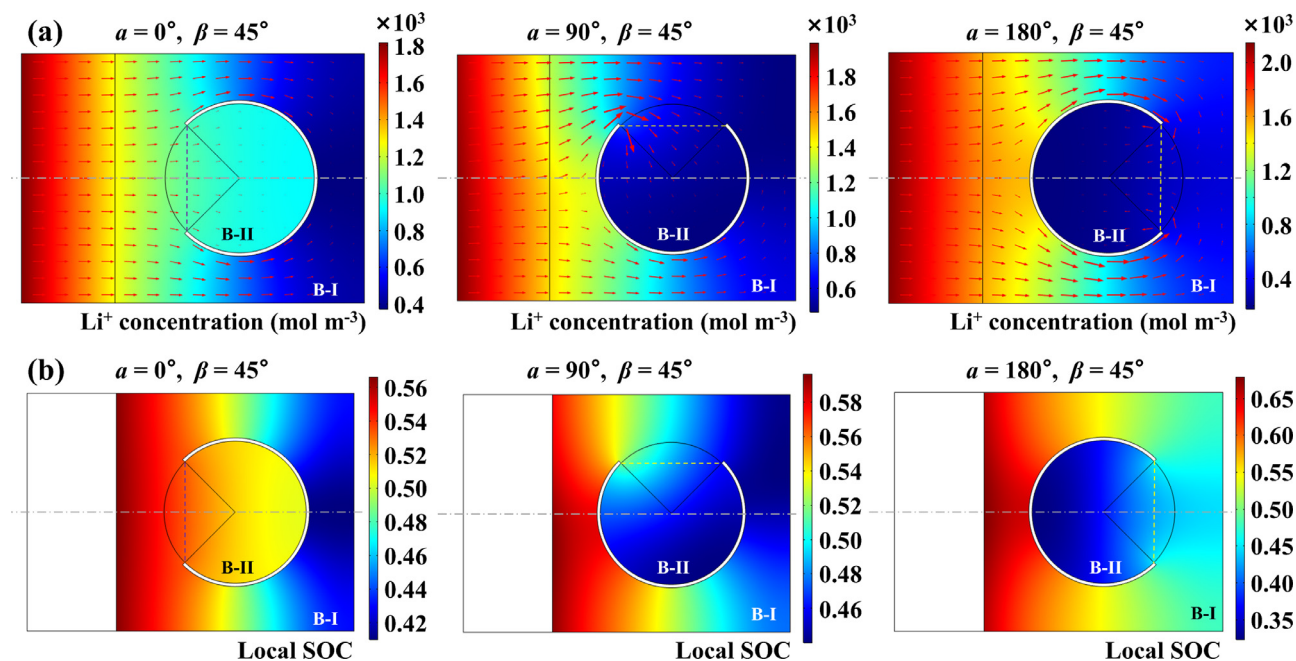


Fig. 17. (a) The contours of lithium ion concentration in the electrolyte for various crack opening directions. (b) The contours of local SOC in the cathode for various crack opening directions. ($i_{app} = 50 \text{ A m}^{-2}$, average cathode SOC: 0.5).

the particles in B-II to be partially intercalated with lithium. These results suggest that despite the identical shape and opening size, the direction of crack opening significantly affects Li blocking.

Next, we consider a series of β values with the crack opening direction fixed along the y-axis ($\alpha = 90^\circ$). The results are presented in Fig. 18. It is seen from Fig. 18a that when the crack

opening is large ($\beta = 135^\circ$), Li ions can easily diffuse along the crack. The Li ion blocking effect by the crack is similar to that of an elliptical-shaped crack with $a/b = 6$. The electrolyte Li ion concentration within the whole cathode region is relatively uniform. When β decreases from 135° to 45° , the increasing difficulty of Li ion diffusing around the crack reduces the Li ion concentration in

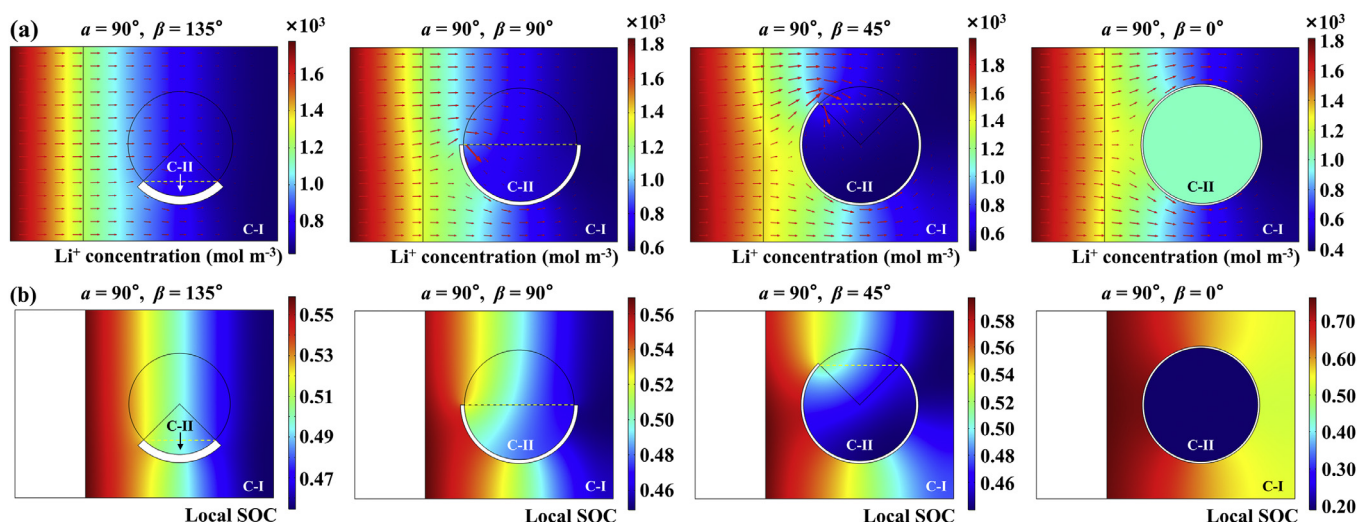


Fig. 18. (a) The contours of lithium ion concentration in the electrolyte for various crack opening sizes. (b) The contours of local SOC in the cathode for various crack opening sizes. (i_{app} : 50 A m^{-2} , average cathode SOC: 0.5)

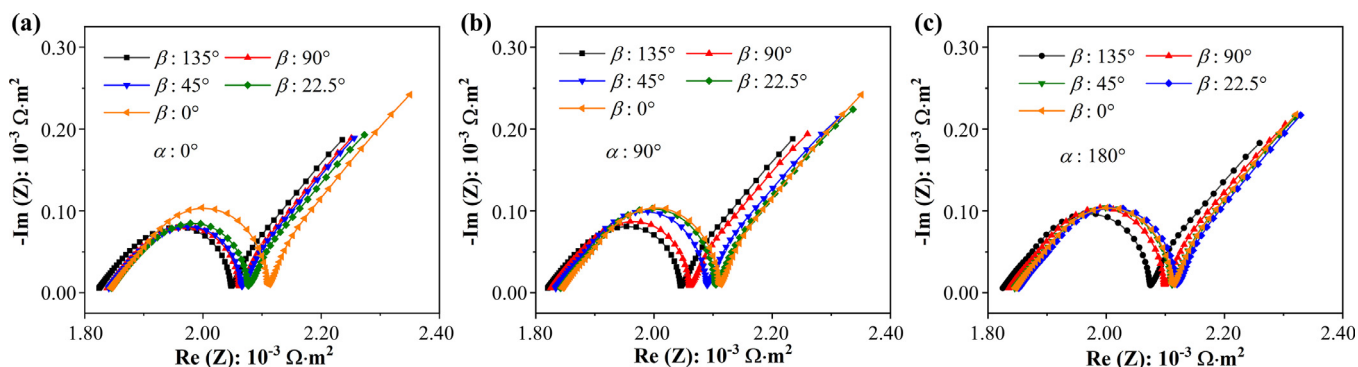


Fig. 19. The impedance spectrum of a cell for various crack opening directions and crack opening sizes. (a) $\alpha = 0^\circ$. (b) $\alpha = 90^\circ$. (c) $\alpha = 180^\circ$. (average cathode SOC: 0.5).

the electrolyte next to the current collector. Near the crack opening, a certain amount of Li ions can diffuse into the enclosed region, but this amount is significantly reduced with a smaller crack opening. The local SOC (Fig. 18b) near the current collector and within the enclosed region significantly decrease when the opening is small, indicating that material there are underuse. This leads to reduced specific energy and specific capacity. When the opening is closed, the material enclosed by the ring-shaped crack is completely isolated, so that it does not contribute to energy storage anymore. This results in a large decrease of specific energy and specific capacity.

The EIS simulations for various crack opening sizes and directions are shown in Fig. 19, with the crack opening direction α being 0° , 90° and 180° , and the crack opening β being 0° , 22.5° , 45° , 90° , and 135° .

With the crack opening toward the separator ($\alpha = 0^\circ$), the radius of the semi-circle or charge transfer resistance increases slightly when β decreases from 135° to 22.5° (Fig. 19a). This is consistent with the increasing Li ion blocking. The charge transfer resistance increases rapidly as the crack opening decreases to $\beta = 0^\circ$. With the crack opening direction toward the current collector ($\alpha = 180^\circ$), the charge transfer resistance remains almost constant with decreasing crack opening (Fig. 19c), and the resistance is close to the maximum value at $\beta = 0^\circ$, implying that due to significant blocking, it is difficult for Li ions to intercalate into the particles in the B-II region shown in Fig. 17. By contrast,

when the crack opening direction is $\alpha = 90^\circ$, the charge transfer resistance gradually increases with the crack opening. Besides, the ohmic resistance increases when the crack opening decreases from $\beta = 135^\circ$ to 0° . This increase is larger when the crack opening direction changes from toward the separator to toward the current collector, indicating that the electrolyte resistance is affected by the crack opening direction and size.

5. Conclusions

In this research, the effect of electrode-level crack geometrical characteristics on the Li ion battery performances and impedance are quantitatively investigated. With an elliptical-shaped crack, the effect of crack semi-axis length ratio, crack angle, and crack position on the cell performance and impedance are analyzed. Additionally, the impact of geometrical parameters of a ring-shaped crack on cell performance and impedance is obtained. The conclusions include the following.

- (1) The mechanism that a crack affects the cell performance is by blocking Li ion transport. The geometrical characteristics of a crack can lead to various blocking effects, causing non-uniform Li ion distribution in the electrolyte and non-uniform SOC in the cathode. Increasing discharge current density further aggravates the impact.
- (2) An elliptical-shaped crack that is longer and more parallel to the current collector (in terms of crack angle) reduces

the specific energy and specific capacity more. The effect is large when the current density is high. For instance, with $a/b = 0.05$ at $i_{app} = 100 \text{ A m}^{-2}$, the specific energy and specific capacity are both reduced by more than 1/3 relative to those of a crack perpendicular to the current collector. A crack perpendicular to the current collector has little impact on cell performance. A crack closer to the separator dramatically reduces the specific energy and specific capacity, especially when the crack is long and is under large discharge current densities. For instance, with $a/b = 0.05$ and $i_{app} = 100 \text{ A m}^{-2}$, the specific energy and specific capacity at $d = 70 \text{ }\mu\text{m}$ are both about 280% higher than those at $d = 10 \text{ }\mu\text{m}$. These results suggest that cracks parallel to the current collector and close to the separator should receive special attention in experimental analysis.

- (3) For an elliptical-shaped crack, the shape factors such as semi-axis ratio, crack angle and wetting ratio affect primarily the ohmic resistance. A longer crack more parallel to the current collector increases the ohmic resistance, while more crack wetting reduces the ohmic resistance. By contrast, crack position significantly affects the charge transfer resistance with little impact on the ohmic resistance. A crack closer to the separator significantly increases the charge transfer resistance.
- (4) A ring-shaped crack with a smaller opening reduces the specific energy and specific capacity more. When the opening is closed, the material enclosed by the ring-shaped crack is completely isolated, so that it does not contribute to energy storage anymore. This results in a large decrease of specific energy and specific capacity. When the crack opening faces the separator, the specific energy and specific capacity are initially insensitive to decreasing opening sizes, but drops rapidly when the opening size is sufficiently small (e.g. $\beta < 22.5^\circ$). By contrast, when the crack opening faces the current collector, the specific energy and specific capacity decrease instantly but more gradually with decreasing opening sizes. Eventually, regardless of the crack opening direction, the specific energy (or specific capacity) reduces to the same value when the opening decreases to be completely closed. When the crack opening faces the separator, the charge transfer resistance increases with reducing opening size, while when the crack opening faces the current collector, the charge transfer resistance does not change much. The ohmic resistance increases when the crack opening decreases.

These results will inform electrode structure design, cell manufacturing and the charge/discharge management system the significance of avoiding crack formation, especially near the separator and parallel to the current collector, and to avoid closed cracks that lead to material isolation. Crack formation is related to stress generation. In electrode design, reducing the gradient of lithium ion concentration in the electrolyte and improving the uniformity of the state of charge in the electrode, especially in regions near the separator, help reduce the stress caused by the non-uniform electrode deformation during lithium ion intercalation/deintercalation. These further reduce the risk of crack nucleation and spreading. For instance, 3D structures such as electrolyte channels can be introduced in the electrode to reduce the stress near the separator [8]. In cell manufacturing, the strategy is to reduce manufacturing defects (such as voids, delamination and microcracks) to avoid crack near the separator or crack growth along the more detrimental directions parallel to the current collector. Inspection strategies can be developed to look for those more harmful crack precursors at the location and direction of interest. For designing better charge/discharge strategies, it is important to introduce physics-

based crack growth models predicting the effect of operational conditions on the crack characteristics (such as growth direction and growth rate) into control decisions. Besides, novel algorithms can be developed to monitor the impedance of battery cells during usage, integrating with the crack growth model, to provide information to the battery management system. These can help optimize and dynamically update control profiles to reduce battery degradation.

Declaration of Competing Interest

The authors declare that they have no known competing financial interests or personal relationships that could have appeared to influence the work reported in this paper.

CRediT authorship contribution statement

Tianhan Gao: Formal analysis, Methodology, Investigation, Data curation, Visualization, Writing - original draft. **Andrew Kim:** Methodology, Writing - original draft. **Wei Lu:** Conceptualization, Methodology, Writing - review & editing, Resources, Funding acquisition, Supervision.

Acknowledgment

The authors gratefully acknowledge the support by the National Science Foundation under Grant No. [CNS-1446117](#) and by LG Chem.

Appendix A. The electrochemical parameters used in this research

[Table A1](#) and [Fig. A1](#)

Table A1
Values of electrochemical parameters used in simulations.

| Parameter | Symbol | Value |
|---------------|---|--|
| $C_{s,max}$ | Maximum lithium ion concentration in cathode particle | 24161 mol m^{-3} |
| D_{e0} | Diffusivity of lithium ion in bulk electrolyte | $7.5 \times 10^{-11} \text{ m}^2 \text{ s}^{-1}$ |
| D_s | Diffusivity of lithium ion in cathode particle | $1 \times 10^{-14} \text{ m}^2 \text{ s}^{-1}$ |
| F | Faraday constant | 96485 C mol^{-1} |
| K | Reaction rate constant for cathode | $5 \times 10^{-10} \text{ m}^{2.5} \text{ mol}^{-0.5} \text{ s}^{-1}$ |
| K_{Li} | Lithium deposition rate coefficient | $6.1 \times 10^{-6} \text{ m}^{-0.5} \text{ mol}^{0.5} \text{ s}^{-1}$ |
| r_p | Cathode particle radius | $5 \text{ }\mu\text{m}$ |
| R | Ideal gas constant | $8.3145 \text{ J mol}^{-1} \text{ K}^{-1}$ |
| t_+ | Lithium ion transference number | 0.363 |
| T | Temperature | 298 K |
| α | Anodic charge transfer coefficient in cathode | 0.5 |
| β | Charge transfer coefficient for lithium deposition | 0.5 |
| κ_{e0} | Bulk electrolyte conductivity | Ref. [3] |
| σ_{s0} | Bulk solid phase electronic conductivity in cathode | 10 S m^{-1} |

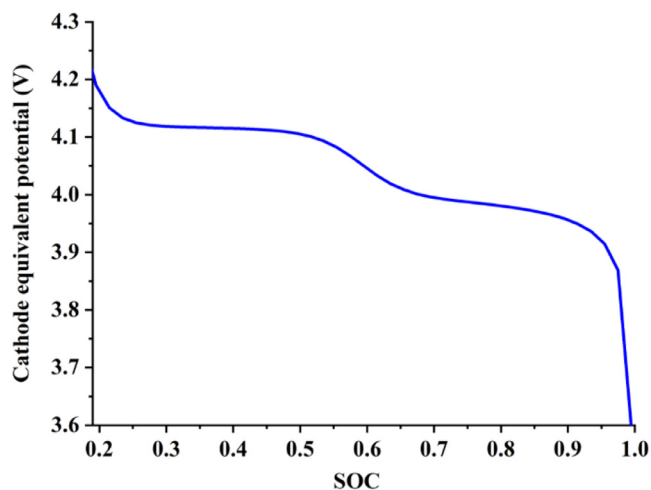


Fig. A1. The equilibrium potential of the cathode material (LiMn_2O_4).

References

- [1] T. Gao, W. Lu, Mechanism and effect of thermal degradation on electrolyte ionic diffusivity in Li-ion batteries : a molecular dynamics study, *Electrochim. Acta* 323 (2019) 134791, doi:10.1016/j.electacta.2019.134791.
- [2] B. Ravdel, K.M. Abraham, R. Gitzendanner, J. DiCarlo, B. Lucht, C. Campion, Thermal stability of lithium-ion battery electrolytes, *J. Power Sources* 119–121 (2003) 805–810, doi:10.1016/S0378-7753(03)00257-X.
- [3] X. Lin, J. Park, L. Liu, Y. Lee, A.M. Sastry, W. Lu, A comprehensive capacity fade model and analysis for Li-Ion batteries, *J. Electrochem. Soc.* 160 (2013) A1701–A1710, doi:10.1149/2.040310jes.
- [4] Y.K. Lee, J. Park, W. Lu, A comprehensive experimental and modeling study on dissolution in Li-Ion batteries, *J. Electrochem. Soc.* 166 (2019) A1340–A1354, doi:10.1149/2.0111908jes.
- [5] G. Liu, W. Lu, A model of concurrent lithium dendrite growth, SEI growth, SEI penetration and regrowth, *J. Electrochem. Soc.* 164 (2017) A1826–A1833, doi:10.1149/2.0381709jes.
- [6] L. Chen, H.W. Zhang, L.Y. Liang, Z. Liu, Y. Qi, P. Lu, J. Chen, L.Q. Chen, Modulation of dendritic patterns during electrodeposition: a nonlinear phase-field model, *J. Power Sources* 300 (2015) 376–385, doi:10.1016/j.jpowsour.2015.09.055.
- [7] V. Yurkiv, T. Foroozan, A. Ramasubramanian, R. Shahbazian-Yassar, F. Mashayek, Phase-field modeling of solid electrolyte interface (SEI) influence on Li dendritic behavior, *Electrochim. Acta* 265 (2018) 609–619, doi:10.1016/j.electacta.2018.01.212.
- [8] T. Gao, W. Lu, Physical model and machine learning enabled electrolyte channel design for fast charging, *J. Electrochem. Soc.* (2020), doi:10.1149/1945-7111/aba096.
- [9] D. Gruet, B. Delobel, D. Sicsic, I.T. Lucas, V. Vivier, On the electrochemical impedance response of composite insertion electrodes—Toward a better understanding of porous electrodes, *Electrochim. Acta* 295 (2019) 787–800.
- [10] S.Y. Lee, Y. Choi, S.H. Kwon, J.S. Bae, E. Duck Jeong, Cracking resistance and electrochemical performance of silicon anode on binders with different mechanical characteristics, *J. Ind. Eng. Chem.* 74 (2019) 216–222, doi:10.1016/j.jiec.2019.03.009.
- [11] V.M. Nagulapati, Y.H. Yoon, D.S. Kim, H. Kim, W.S. Lee, J.H. Lee, K.H. Kim, J. Hur, I.T. Kim, S.G. Lee, Effect of binders and additives to tailor the electrochemical performance of Sb_2Te_3 -TiC alloy anodes for high-performance sodium-ion batteries, *J. Ind. Eng. Chem.* 76 (2019) 419–428, doi:10.1016/j.jiec.2019.04.008.
- [12] V.M. Nagulapati, D.S. Kim, J. Oh, J.H. Lee, J. Hur, I.T. Kim, S.G. Lee, Enhancing the electrochemical performance of SbTe bimetallic anodes for high-performance sodium-ion batteries: Roles of the binder and carbon support matrix, *Nano-materials* 9 (2019) 1–17, doi:10.3390/nano9081134.
- [13] J. Kumberg, M. Müller, R. Diehm, S. Spiegel, C. Wachsmann, W. Bauer, P. Scharfer, W. Schabel, Drying of lithium-ion battery anodes for use in high-energy cells: influence of electrode thickness on drying time, adhesion, and crack formation, *Energy Technol.* (2019) 7, doi:10.1002/ente.201900722.
- [14] B. Lu, C. Ning, D. Shi, Y. Zhao, J. Zhang, Review on electrode-level fracture in lithium-ion batteries, *Chin. Phys. B* 29 (2020) 026201, doi:10.1088/1674-1056/ab6841.
- [15] Y. Zhang, C. Zhao, Z. Guo, Simulation of crack behavior of secondary particles in Li-ion battery electrodes during lithiation/de-lithiation cycles, *Int. J. Mech. Sci.* 155 (2019) 178–186, doi:10.1016/j.jmecs.2019.02.042.
- [16] M. Klinsmann, D. Rosato, M. Kamlah, R.M. McMeeking, Modeling crack growth during Li insertion in storage particles using a fracture phase field approach, *J. Mech. Phys. Solids* 92 (2016) 313–344, doi:10.1016/j.jmps.2016.04.004.
- [17] A.A. Tahmasbi, M.H. Eikerling, Statistical physics-based model of mechanical degradation in lithium ion batteries, *Electrochim. Acta* 283 (2018) 75–87.
- [18] V. Vanpeene, A. Etienne, A. Bonnin, E. Maire, L. Roué, In-situ X-ray tomographic study of the morphological changes of a Si/C paper anode for Li-ion batteries, *J. Power Sources* 350 (2017) 18–27, doi:10.1016/j.jpowsour.2017.03.044.
- [19] S. Lee, J. Yang, W. Lu, Debonding at the interface between active particles and PVDF binder in Li-ion batteries, *Extrem. Mech. Lett.* 6 (2016) 37–44, doi:10.1016/j.eml.2015.11.005.
- [20] T.K. Bhandakkar, H. Gao, Cohesive modeling of crack nucleation under diffusion induced stresses in a thin strip: Implications on the critical size for flaw tolerant battery electrodes, *Int. J. Solids Struct.* 47 (2010) 1424–1434, doi:10.1016/j.ijsolstr.2010.02.001.
- [21] M.A. Rahman, C. Wen, A study of the capacity fade of porous NiO/Ni foam as negative electrode for lithium-ion batteries, *Ionics* (Kiel) 22 (2016) 173–184, doi:10.1007/s11581-015-1542-8.
- [22] Y. Wang, D. Dang, D. Li, J. Hu, X. Zhan, Y.T. Cheng, Effects of polymeric binders on the cracking behavior of silicon composite electrodes during electrochemical cycling, *J. Power Sources* 438 (2019) 226938, doi:10.1016/j.jpowsour.2019.226938.
- [23] Y. Zhao, J. Wang, Q. He, J. Shi, Z. Zhang, X. Men, D. Yan, H. Wang, Li-ions transport promoting and highly stable solid-electrolyte interface on Si in multilayer Si/C through thickness control, *ACS Nano* 13 (2019) 5602–5610, doi:10.1021/acsnano.9b00670.
- [24] D. Grazioli, O. Verners, V. Zadin, D. Brandell, A. Simone, Electrochemical-mechanical modeling of solid polymer electrolytes: impact of mechanical stresses on Li-ion battery performance, *Electrochim. Acta* 296 (2019) 1122–1141.
- [25] H. Qu, J. Kaffle, J. Harris, D. Zheng, J. Koshina, D. Boone, A.M. Drake, C.J. Abeglen, D. Qu, Application of ac impedance as diagnostic tool—low temperature electrolyte for a Li-ion battery, *Electrochim. Acta* 322 (2019) 134755.
- [26] M. Doyle, Modeling of galvanostatic charge and discharge of the lithium/polymer/insertion cell, *J. Electrochem. Soc.* 140 (1993) 1526, doi:10.1149/1.2221597.
- [27] T.M. Clancy, J.F. Rohan, Simulations of 3D nanoscale architectures and electrolyte characteristics for Li-ion microbatteries, *J. Energy Storage* 23 (2019) 1–8, doi:10.1016/j.est.2019.02.002.
- [28] L. Yang, H. Sen Chen, H. Jiang, W.L. Song, D. Fang, Lithium redistribution around the crack tip of lithium-ion battery electrodes, *Scr. Mater.* 167 (2019) 11–15, doi:10.1016/j.scriptamat.2019.03.033.
- [29] R. Xu, K. Zhao, Corrosive fracture of electrodes in Li-ion batteries, *J. Mech. Phys. Solids* 121 (2018) 258–280, doi:10.1016/j.jmps.2018.07.021.
- [30] Y.F. Gao, M. Zhou, Coupled mechano-diffusional driving forces for fracture in electrode materials, *J. Power Sources* 230 (2013) 176–193, doi:10.1016/j.jpowsour.2012.12.034.
- [31] Y. Bie, J. Yang, W. Lu, Z. Lei, Y. Nuli, J. Wang, A facile 3D binding approach for high Si loading anodes, *Electrochim. Acta* 212 (2016) 141–146, doi:10.1016/j.electacta.2016.06.152.